Vilnius University
Faculty of Physics
Laser Research Center

Adomas Petrauskas

ANALYSIS OF ULTRASHORT PULSE TEMPORAL CHARACTERISTICS IN A HYBRID LASER WITH A FIBER SEED SOURCE

Master’s final thesis

Laser Physics and Optical Technologies study programme

Student	Adomas Petrauskas
Approved	2026-05-22
Academic supervisor	dr. Tadas Bartulevičius
Consultant	dr. Vaida Marčiulionytė
Director of the Center	dr. Dalia Kaškelytė

Vilnius 2026

Table of Contents

List of Abbreviations

ASE	amplified spontaneous emission
CE	contrast enhancement
CFBG	chirped fiber Bragg grating
CPA	chirped pulse amplification
CR	compression ratio
FCPA	fiber chirped pulse amplification
FROG	frequency-resolved optical gating
FWHM	full width at half maximum
GD	group delay
GDD	group delay dispersion
HCF	hollow-core fiber
MFD	mode field diameter
MOPA	master oscillator power amplifier
MPC	multi-pass cell
NER	nonlinear elliptical rotation
OPA	optical parametric amplification
OPN	optical parametric noise
PMT	photomultiplier tube
SESAM	semiconductor saturable absorber mirror
SHG	second-harmonic generation
SPM	self-phase modulation
TC	temporal contrast
THG	third-harmonic generation
TL	transform-limited
TOD	third-order dispersion
XPW	cross-polarized wave generation
YDF	ytterbium-doped fiber

Introduction

Ultrashort laser pulses with durations in the femtosecond regime (10^{-15} s) play a crucial role in a wide range of scientific and technological applications, from high-intensity laser–matter interaction studies to precision material processing. Generating ultrashort pulses requires gain media with sufficiently broad amplification bandwidths to support the required spectral widths. In femtosecond laser systems, active media include titanium–sapphire (Ti:sapphire) crystals, ytterbium (Yb)–doped solid-state crystals, or Yb-doped optical fibers. Ti:sapphire is characterized by an exceptionally broad gain bandwidth, enabling the generation of ultrashort optical pulses on the order of 10 femtoseconds [1,2] in the Kerr-lens mode-locked configuration. In contrast, Yb-doped solid-state crystals exhibit a narrower gain bandwidth, which results in pulses on the order of a few hundred femtoseconds. However, Yb-doped media benefit from a low quantum defect between the pump and laser wavelengths, leading to high optical efficiency and reduced thermal load [3,4]. Furthermore, the high surface-to-volume ratio of Yb-doped fibers (YDF) provides superior thermal management and structural flexibility compared to bulk crystal geometries [5]. These features enable power-scalable operation and high average output powers while maintaining good beam quality, which is particularly advantageous in high-repetition-rate ultrafast lasers.

To simultaneously achieve high pulse energy and ultrashort pulse duration, chirped-pulse amplification (CPA) techniques are widely employed in modern ultrafast laser systems and provide pulse durations reaching the few-femtosecond regime. Apart from pulse duration, the temporal quality of the pulse, commonly expressed through temporal contrast (TC), is of great importance for many applications. TC is typically defined as the ratio of the main pulse peak intensity to the intensity of pre-pulses, post-pulse, or the temporal background. High TC is essential in high-intensity laser-matter experiments, such as plasma interaction studies [6–8], where even weak pre-pulses can induce unwanted ionization or premature plasma formation, thereby significantly affecting the interaction of the main pulse with the target. To achieve high pulse energy and maintain temporal pulse quality, some femtosecond CPA systems employ a hybrid fiber-solid-state architecture. For example, pulse shaping and pre-amplification may be implemented in a fiber-based seed source, followed by power amplification in solid-state gain media. Within this architecture, the seed pulse generation and initial amplification stage is typically realized in Yb-doped optical fibers, which provide high power efficiency and mechanical stability, while final amplification to higher pulse energies occurs in solid-state crystals such as Yb:YAG, Yb:KGW, or Yb:CALGO [9,10]. By combining fiber and solid-state amplification stages, the hybrid architecture enables scaling to high average powers while preserving broad spectral bandwidth and mitigating the nonlinear effects that often degrade pulse quality in all-fiber chirped-pulse amplification (FCPA) systems.

Among the nonlinear processes affecting temporal pulse quality in the fiber-based systems, self-phase modulation (SPM) plays a key role, as it induces intensity-dependent phase modulation, leading to spectral broadening and accumulation of nonlinear phase φ_{NL}, commonly quantified by the B-integral. It is widely accepted that, when the B-integral exceeds a threshold on the order of ~1π rad [11], significant spectral modulation occurs, leading to visible temporal distortions in the compressed pulse, such as pulse pedestal or satellite structures. In addition to SPM, other mechanisms, including higher-order dispersion, self-steepening, and nonlinear scattering, further degrade the spectral and temporal pulse characteristics at high power levels [12]. Therefore, achieving ultrashort pulses with high temporal quality in fiber-based systems requires careful consideration of both nonlinear effects and system limitations imposed by optical components.

In particular, effective dispersion management is essential, as the accumulated dispersion during pulse stretching must be accurately compensated in the compressor to obtain near-transform-limited pulses. However, dispersive elements such as chirped fiber Bragg gratings (CFBGs) often exhibit fabrication-induced imperfections in their reflectivity and group delay profiles. These imperfections may introduce spectral phase distortions that cannot be fully compensated by the compressor, thereby limiting the achievable temporal contrast.

This study aims to characterize a hybrid CPA system with a fiber seed source and incorporate an improved-quality chirped fiber Bragg grating (CFBG) pulse stretcher to assess the impact of lower reflectivity and group delay ripples on the quality of the compressed pulse.

The objectives of this study are as follows:

1. Measure the temporal profile and evaluate the temporal contrast of the pulses generated by the hybrid CPA system using a high-dynamic-range third-order autocorrelator.
2. Examine the impact of reflectivity and group-delay ripples of the CFBG pulse stretcher on the temporal quality of the compressed pulse.
3. Reduce output pulse duration via post-compression and investigate the influence of CFBG quality on the temporal characteristics of sub-60 fs pulses through third-order autocorrelation measurements and pulse envelope reconstruction using the frequency-resolved optical gating (FROG).
4. Alternatively, evaluate the effectiveness of an external temporal contrast enhancement method based on Kerr lens filtering.

1. Literature Review

1.1. Fiber and hybrid high-average-power ultrashort pulse laser systems

Fiber-based and hybrid ultrashort pulse lasers are sources capable of generating picosecond (ps) to femtosecond (fs) pulses, typically delivering average output powers from several watts to several hundred watts and operating at high pulse repetition rates of several to tens of megahertz (MHz). One of the key advantages of optical fibers in high-average-power systems is their favourable thermal properties and their ability to preserve high spatial beam quality. Owing to their high surface-area-to-volume ratio, optical fibers efficiently dissipate heat generated during amplification due to the quantum defect. This is particularly beneficial for high-repetition-rate systems, where the generated heat is distributed over a large volume, reducing the need for complex thermal management and minimizing beam distortions. Furthermore, the geometry of single-mode fibers inherently helps to mitigate thermally induced mechanical stress and the associated degradation of beam quality, as light is guided by total internal reflection within the fiber core. As a result, the output beam from a single-mode fiber-based source can remain close to diffraction-limited Gaussian propagation ($M^2 \approx 1$) even at high average power levels.

Hybrid laser systems are commonly based on the master power amplifier (MOPA) architecture, in which low-intensity ultrashort pulses generated by an oscillator are subsequently amplified in solid-state media or in optical fibers doped with rare-earth ions (Yb^{3+}, Nd^{3+}, Er^{3+}, Tm^{3+}). The performance of modern hybrid laser systems meets many requirements for applications such as ultrafast spectroscopy and precision material processing due to the range of parameters achievable in this configuration. Pulse durations can reach below 100 femtoseconds and, in some systems, be tuned over a wide range from tens of femtoseconds to a few picoseconds [13,14].

The pulse repetition rate can be readily tuned from single-shot operation to values exceeding 10 MHz. In advanced systems, hybrid CPA setups can deliver average output powers up to 100 W-level [15], while high-energy systems operating at kHz repetition rates may reach pulse energies up to 10 mJ [16]. Such systems typically generate the fundamental harmonic at wavelengths of 1030 nm or 1064 nm (corresponding to Yb- or Nd-doped active media, respectively), which can be converted into higher-order harmonics using nonlinear crystals. This enables smaller focal spot sizes and more efficient ablation when processing materials such as silicon [17] and other wide bandgap materials [18].

Compared with fiber-based laser systems, solid-state lasers based on pulse amplification in crystalline media exhibit several fundamental differences. Although solid-state lasers offer high output energy potential, they often suffer from heat accumulation in the crystals and require more complex cooling systems. The quality of the output beam is mainly affected by thermal gradients induced by the pump radiation. For a given crystal geometry, regions of increased mechanical stress can form, which in turn modify the local refractive index and induced polarization rotation of the propagating beam. Since laser systems are typically polarization-selective, depolarization causes beam distortion, reducing output energy and degrading output beam quality. As mentioned above, such losses can be avoided in fiber-based oscillators and amplifiers, where spatial beam cleaning occurs during propagation in the fiber core. In addition, fiber-based systems are attractive due to their stable operation [19,20] and mechanical robustness under varying environmental conditions. This is more difficult to achieve in solid-state resonators, which rely on precise mechanical alignment of optical elements; furthermore, optical components may become contaminated, posing a risk to long-term reliability of the system.

1.1.1. Evolution of ultrashort pulse parameters in a fiber CPA system

Pulses generated in a fiber oscillator exhibit certain limitations in both minimum achievable duration and subsequent energy scaling. The spectrum of pulses generated by the oscillator is typically narrow and is further shaped using various techniques. One of the key stages in FCPA systems is spectral broadening. This can be achieved in a single-mode fiber characterized by a given nonlinear refractive index n_2. Due to the intensity-dependent refractive index, the pulse acquires a time-dependent phase. Since the instantaneous frequency is given by the temporal derivative of the phase, this results in a shift of the carrier frequency:

$$\delta\omega = -\frac{\omega_0 z}{c} n_2^I \frac{dI}{dt}. \quad (1)$$

It follows that the intensity-dependent refractive index induces frequency modulation of the pulse, a process known as self-phase modulation (SPM). This effect generates new frequency components at the spectral edges, thereby broadening the pulse spectrum. Consequently, from the Fourier transformation, a shorter transform-limited (TL) pulse duration can be achieved. Equation (1) indicates that, in addition to the nonlinear refractive index of the medium, the spectral broadening is governed by the total length of the nonlinear medium z, the pulse intensity I, and the pulse duration t. Thus, by controlling these quantities, the spectral broadening may result in different spectral intensity shapes, such as flat-top or triangular profiles [21]. In certain cases, a parabolic spectral shape is targeted, as it enables efficient amplification without wave breaking [22], a process in which nonlinear effects significantly distort the pulse shape.

Following the spectral broadening, dispersive pulse stretching is applied to reduce pulse intensity before amplification. The theoretical basis of pulse stretching can be described in terms of the spectral phase, which is related to the wave vector $k(\omega) = \omega n(\omega)/c$ through the relation:

$$\varphi(\omega, z) = \omega \cdot n(\omega) \cdot {}^{z}/_{c} \quad (2)$$

Here: n – the refractive index, c – the speed of light, ω – the carrier angular frequency, and z – the propagation distance. The spectral phase function defines the phase shift accumulated by each frequency component during propagation. This function is typically analyzed by performing a Taylor series expansion around the carrier angular frequency ω_0:

$$\varphi(\omega, z) = \varphi(\omega_0, z) + \frac{d\varphi(\omega,z)}{d\omega} \cdot (\omega - \omega_0) + \frac{1}{2}\frac{d^2\varphi(\omega,z)}{d\omega^2} \cdot (\omega - \omega_0)^2 + \frac{1}{6}\frac{d^3\varphi(\omega,z)}{d\omega^3} \cdot (\omega - \omega_0)^3 + \cdots \quad (3)$$

From this expansion, the derivatives of the spectral phase are obtained, each having a corresponding physical meaning and notation:

$$GD = \frac{d\varphi(\omega,z)}{d\omega}, \quad (4)$$

$$GDD = \frac{d^2\varphi(\omega,z)}{d\omega^2}, \quad (5)$$

$$TOD = \frac{d^3\varphi(\omega,z)}{d\omega^3}, \quad (6)$$

Here, GD denotes group delay, GDD denotes group delay dispersion, and TOD denotes third-order dispersion. Each derivative term of the spectral phase influences the temporal shape of the pulse after propagation over a given distance in a medium. In the dispersion management of ultrashort pulses, GDD usually plays the dominant role, as it is used to introduce a linear chirp, corresponding to a quadratic spectral phase. On the other hand, to achieve high compressed pulse quality, particularly for pulses with durations below a hundred femtoseconds, compensation of third-order and higher-order dispersion becomes necessary.

1.1.2. The impact of fiber amplifier on pulse temporal characteristics

The output pulse quality is heavily determined by the nonlinear phase shift accumulated in the fiber amplifier, denoted as Φ_{NL}. The optical Kerr effect arises from the cubic nonlinear polarization response of a medium, described by the third-order nonlinear susceptibility $\chi^{(3)}$. The refractive index experienced by the spectral components becomes dependent on the instantaneous light intensity. Consequently, at sufficient propagating pulse intensity, the temporal phase is modified, leading to SPM. The nonlinear phase shift accumulated over a distance L, also referred to as the B-integral, can be described as follows:

$$\phi_{NT}(z) = B = \frac{2\pi}{\lambda} n_2 \int_0^L I(z)\, dz. \quad (7)$$

The effect of the medium on the propagating wave can be characterized by the nonlinearity parameter γ (gamma) (8), which incorporates the nonlinear refractive index n_2, wavelength λ, and effective mode area A_{eff} of the fiber:

$$\gamma = \frac{2\pi n_2}{\lambda\, A_{eff}}. \quad (8)$$

It is important to note that, in the case of optical fibers, the effective mode area through which the laser radiation propagates is calculated as $A_{eff} = \pi \left(\frac{MFD}{2}\right)^2$, where MFD is the mode field diameter. The MFD differs from the physical core diameter as it accounts for the evanescent field (the decaying light intensity) at the core-cladding interface. Furthermore, the MFD depends on both the wavelength of the propagating wave and the refractive index profile of the fiber. Thus, the equation for the accumulated nonlinear phase, or B-integral, can be simplified using the nonlinearity (8) parameter, where P(z) represents the peak pulse power:

$$B = \int_0^L \gamma P(z)\, dz \quad (9)$$

Once the accumulated nonlinear phase exceeds a critical threshold (typically $\Phi_{NL} > 1\pi$ rad), pulses begin to significantly deform spectrally and temporally. This leads to spectral modulations that degrade the compressed pulse shape and limit the minimum achievable pulse duration. Therefore, when designing CPA systems, it is critical to optimize both fiber length and gain level (pulse intensity) to ensure sufficient amplification while minimizing nonlinear effects. In practice, higher ultrashort pulse energies are achieved by employing a hybrid amplification scheme that combines fiber and solid-state amplifiers [9].

1.1.3. Influence of the CFBG quality on the temporal characteristics of the compressed pulses

Dispersion in CPA systems can be introduced using free-space optical elements, such as diffraction gratings or prism pairs, while fiber-based systems commonly employ CFBGs [23]. The operation of these dispersive elements is based on Bragg reflection at optical interfaces with different refractive indices. Similar to a conventional Bragg mirror, a refractive index modulation is periodically inscribed in the fiber core. However, in a CFBG, the grating period varies along the fiber, so the condition for constructive reflection is met at different positions for different wavelengths. The control of the refractive index modulation during inscription enables adjustment of the dispersion introduced by the component. An advantage of these stretchers is that the second- and higher-order dispersion can be tailored during inscription to match and compensate for the dispersion of the pulse compressor.

It is important to note that the inscription of CFBG is a technically demanding process prone to various manufacturing inaccuracies. These imperfections can lead to spectral amplitude modulations (known as spectral ripples) in the grating's response, which cause an undesirable redistribution of energy in the time domain, resulting in a temporal pedestal or the formation of satellite pulses at the pulse periphery [24]. Furthermore, phase inscription errors – arising from fiber core inhomogeneities, impurities, and the limited precision of fabrication methods or equipment – can induce group delay ripples. These ripples manifest as high-frequency spectral phase modulations, which degrade the quality of pulse compression [25,26]. Consequently, in CPA systems, the use of dispersive components with such manufacturing defects often leads to inferior temporal pulse quality. The process is discussed in more detail in the experimental section 3.2.

1.2. Temporal contrast in ultrafast laser systems

The temporal contrast of an ultrashort laser pulse is a critical characteristic that defines its pulse shape and practical utility. It represents the ratio between the peak intensity of the main pulse and the intensity of any preceding or trailing background structures. In an ideal scenario, all energy is contained within the main pulse, with the surrounding background being negligibly small.

In practical-world, however, several factors degrade pulse quality. First, the temporal shape can be distorted by the accumulation of nonlinear phase shifts (discussed in Section 1.1.1) or by higher-order dispersion that remains uncompensated by the pulse compressor. Additionally, active gain media generate amplified spontaneous emission (ASE). Unlike dispersion-induced distortions, ASE background is non-coherent and typically spans a broad temporal range of hundreds of picoseconds around the main pulse, forming an incoherent energy background.

Temporal pulse quality can be quantified in several ways. One commonly used method is the Strehl ratio, which describes the ratio between the measured peak intensity and the peak intensity of an ideal TL pulse. Alternatively, a temporal contrast (TC) is defined as the ratio of the main pulse intensity to the surrounding background intensity. These metrics are essential for evaluating temporal quality, which strongly depends on the specific design of the laser system.

1.2.1. Role of pulse temporal contrast in ultrafast laser applications

The TC parameter becomes particularly significant in high-intensity ultrashort pulse laser systems [27–29]. In such systems, even extremely weak temporal structures preceding the main pulse may carry enough energy to cause undesirable interactions with matter. Consequently, temporal contrast directly dictates the precision of various laser applications. For instance, in high-intensity interactions with solids or plasma, poor temporal contrast can trigger premature ionization or surface modification, significantly altering the absorption and energy transfer mechanisms of the main pulse. Similarly, in laser-driven particle acceleration and inertial confinement fusion experiments, insufficient contrast can lead to pre-plasma formation, reducing the overall process efficiency. Therefore, high pulse contrast is essential for controlling interaction processes and enabling accurate analysis of physical mechanisms.

In certain cases, the presence of a pulse pedestal at a specific energy level may be advantageous. For example, several studies in laser micromachining have shown that, with appropriate pre-pulse energy, the formation of a pre-plasma can enhance the absorption of the main pulse [30], while the ASE energy background may improve the focusing of the main pulse, leading to more efficient energy transfer to the plasma [31]. Moreover, in laser–matter interaction experiments aimed at controlled surface heating or preconditioning of the material, the energy pedestal can create favourable conditions for uniform energy absorption of the main pulse. One example is silicon modification experiments, where it has been demonstrated that a pre-pulse energy background can enhance material absorption and reduce the processing threshold [32].

1.2.2. Temporal contrast in solid-state CPA systems

In solid-state CPA systems, relatively high TC can be achieved. In many cases, the pulse intensity within the optical components is maintained low enough that the Kerr effect and nonlinear phase accumulation remain negligible. Consequently, the pulses generated in the oscillator are chirped to reduce the intensity and then amplified in the crystalline medium without inducing significant SPM-related distortions. Thus, after dispersion compensation in the pulse compressor, a smooth pulse envelope is obtained. In systems based on Ti:Sapphire active media, which produce pulses shorter than 100 fs, the temporal contrast can reach 10^{-7} – 10^{-9} [33,34], with the ASE of the amplification stage being the primary limiting factor. Since the incoherent energy background of ASE is not phase-locked to the main ultrashort pulse, its contribution cannot be removed by dispersion compensation in the compressor.

In contrast, Yb:YAG systems typically generate slightly longer pulses (approximately 300 fs) due to the narrower gain bandwidth and generally exhibit lower pulse TC. The longer excited-state lifetime of Yb:YAG, which is approximately 1 ms at room temperature [35], compared to ~3 μs for Ti:Sapphire [36], creates more favorable conditions for the accumulation of ASE. Due to the increased ASE background in this configuration, the TC of the compressed pulses is limited to the range of 10^{-5} – 10^{-7} [37].

1.2.3. Limitations of temporal contrast in fiber CPA systems

In contrast, high-power FCPA systems often exhibit lower temporal contrast than typical solid-state lasers. First, ultrashort pulse amplification in optical fibers is characterized by a long effective interaction length and a high small-signal gain coefficient. Consequently, spontaneous emission generated in the active medium is amplified into ASE, forming an incoherent nanosecond-scale energy background. Furthermore, fiber amplifiers maintain tight pulse localization within a small-diameter core and, therefore, high-energy pulses inevitably accumulate a significant nonlinear phase shift (Eq. 7). For these reasons, high-power FCPA systems often achieve inferior compressed pulse TC, with the temporal pedestal level increasing to 10^{-5} or higher levels [32,38]. Thus, in certain cases, the pulses generated by FCPA may not meet the required temporal quality standards, necessitating system optimization or the application of temporal contrast enhancement techniques.

1.2.4. Temporal contrast enhancement methods

The satellite pulses or high incoherent energy background of an ultrashort pulse can be externally filtered using several methods. Due to the low intensity of these temporal structures relative to the main pulse, selective filtering is possible by exploiting nonlinear processes, where the process efficiency depends strongly on the instantaneous electric field intensity. The nonlinear polarization response of a medium is described by higher-order susceptibilities, where $\chi^{(2)}$and $\chi^{(3)}$correspond to polarization terms that scale quadratically and cubically with the incident electric field. Consequently, high-intensity femtosecond pulses undergo nonlinear interaction, while the contribution of low-intensity components remains minimal, enabling temporal filtering. This principle underlies such pulse-cleaning techniques as optical parametric amplification (OPA), cross-polarized wave generation (XPW), and nonlinear elliptical rotation (NER) [39–41]. These methods can be further categorized according to the order of the nonlinear interaction.

The first category comprises second-order nonlinear processes in anisotropic media, which exhibit a quadratic polarization response to the electric field, governed by χ^2 term. A significant advantage of these methods is their applicability at lower pulse intensities, typically in the range of 1–10 GW/cm² [41]. Techniques such as second-harmonic generation (SHG) and OPA can be employed. While SHG is not a direct method for temporal filtering, as it changes the input pulse frequency, it is often utilized as a final stage in multi-step parametric amplification schemes to further suppress the background noise [41,42]. To avoid optical parametric noise (OPN), a pulsed pump source is required, which can be achieved by using a replica of the original ultrashort pulse. Through this process, the temporal contrast can be improved by 10^2 to 10^4 times using one or two nonlinear stages, although the final energy transmission efficiency may decrease to around 10%.

Following, temporal CE can be achieved through nonlinear processes based on third-order nonlinear susceptibility (χ^3), typically requiring pulse intensities on the order of 10^{11} – 10^{12} W/cm^2. While such high intensities can lead to the degradation of spatial beam quality through self-focusing, they enable efficient pulse cleaning in both crystalline and amorphous media, such as inert gases. This category includes cross-polarized wave (XPW) generation, nonlinear ellipse rotation (NER), and techniques utilizing the Kerr effect. XPW generation allows for temporal contrast improvement by several orders of magnitude, although its energy efficiency is generally limited to 20% or less [27,43]. The XPW process involves the generation of a new, linearly polarized wave with an orthogonal orientation to the input pulse through a cubic nonlinear interaction within the crystal, effectively acting as a high-speed optical shutter that transmits only the high-intensity portion of the pulse. It is frequently implemented in BaF_2 crystals by focusing the pulse to intensities near 10^{12} W/cm^2, which often requires rotating or replacing the crystal over long-term operation to mitigate material fatigue. In contrast, the NER method does not generate a new wave; instead, energy is redistributed within the pulse itself, theoretically allowing for significantly higher energy efficiency. The NER method utilizes intensity-dependent nonlinear rotation of the pulse's polarization ellipse, followed by a polarizer that blocks the low-intensity linear background while transmitting the rotated high-intensity peak. This method enables both temporal pulse cleaning and spectral broadening – a critical factor in the generation of few-cycle pulses – with TC improvements typically exceeding 10^2 and efficiencies in modern schemes reaching up to 50% [39,44]. Furthermore, Kerr-nonlinearity-based spectral broadening via self-phase modulation and spectral filtering can be applied. For instance, 1 mJ, ~300 fs pulses generated by an FCPA system can be temporally cleaned using SPM in an argon-filled hollow-core fiber combined with a spectral filter [45].

Alternatively, temporal contrast enhancement (CE) may be achieved via pulse self-focusing and filtering, as demonstrated by Zaharit Refaeli *et al*. [38]. In this work, self-focusing in a Kerr medium was exploited to improve the incident pulse temporal contrast through selective pulse-peak filtering using a fixed aperture. The underlying mechanism relies on the intensity-dependent refractive index of the nonlinear medium. While the low-intensity pedestal and ASE background propagate linearly, the high-intensity peak of the pulse induces a self-focusing effect that modifies its spatial profile and beam divergence. By placing a pinhole or aperture at the plane of nonlinear focus, the system acts as a spatial filter that preferentially transmits the pulse temporal peak while blocking the background temporal features. In a proof-of-concept demonstration, the authors claim to have achieved a CE factor of one to two orders of magnitude. This approach is particularly attractive for high-repetition-rate systems, as it offers a relatively simple, passive setup compared to more complex techniques discussed above.

1.3. Ultrashort pulse post-compression methods

For some ultrashort laser pulse applications, it is necessary to reduce the duration of the output pulses to achieve higher peak intensities than those attainable with CPA systems. One of the most widely implemented methods for achieving shorter pulse durations is the post-compression. The technique typically comprises two distinct stages: first, nonlinear spectral broadening, primarily driven by SPM via the medium's nonlinear polarization response, followed by dispersion compensation, during which the residual dispersion accumulated during the spectral broadening process is compensated to reach a near-transform-limited pulse duration. Such a methodology enables the external shortening of pulses generated by the system without requiring modifications to the existing CPA architecture.

The first group of such methods includes post-compression based on spectral broadening in inert gases. In these systems, nonlinear spectral broadening is primarily driven by the medium's third-order dielectric susceptibility (χ^3). As a result, the propagating pulse undergoes SPM, which generates new frequency components. One common configuration for this method involves broadening the pulse spectrum within an inert gas chamber, which can be designed for either a single-pass interaction [46] or a multi-pass configuration, also known as a Herriott cell [47]. In both cases, an intense laser pulse is focused into a sealed chamber filled with inert gases such as argon, neon, or helium. The strength of the nonlinear interaction in these pulse compressors is controlled by adjusting the gas pressure, pulse energy, and focusing conditions. The acquired dispersion is subsequently compensated using dispersive elements, such as chirped mirrors, prism pairs, or diffraction gratings. Inert-gas-based post–compressors are compatible with a wide range of pulse energies and offer straightforward integration and high energy throughput, making them suitable for high-power laser systems.

Furthermore, spectral broadening in inert gases may be utilized inside a hollow-core fiber (HCF) pulse compressor. In this setup, gas pressure is typically managed by placing the HCF inside a vacuum-tight chamber. The distinct advantage of the HCF-based method is the ability to easily maintain a long interaction length for the pulse inside the medium. By applying HCF pulse compressors, it is possible to achieve pulse durations approaching a few optical cycles [48,49], with compression ratios exceeding a factor of 10 [49].

Post-compressors with a solid-state medium and a multi-pass cell (MPC) design are also widely utilized for external pulse compression. This method creates conditions where the pulse propagates multiple times through a nonlinear medium, often a thin solid-state plate, while the beam path is stabilized by a mirror configuration resembling an optical resonator. MPCs allow for precise control over the number of passes and the cumulative nonlinear phase acquired during propagation. By employing mirrors with high-quality dielectric coatings, these cells can maintain exceptionally high throughput efficiency. This pulse compression technique is particularly attractive for applications requiring stable performance without the active nonlinearity management typically associated with the previously discussed inert gas-filled media.

Both HCF and MPC-based schemes are capable of reaching similar pulse durations of a few optical cycles [50–52]. Ultimately, the choice between these configurations is dictated by the specific requirements regarding system stability and ease of integration.

2. Methodology

2.1. Ultrashort pulse analysis using a second-order autocorrelator

One of the most convenient methods for measuring ultrashort pulses is second-order intensity autocorrelation. Given that the intensity of a light pulse corresponds to the square of the field amplitude ($I(t) \sim |E(t)|^2$), the second-order intensity autocorrelation of two pulses can be described as follows:

$$G^{(2)}(\tau) = \int_{-\infty}^{\infty} I_1(t) I_2(t-\tau) dt, \quad (10)$$

where: I_1 and I_2 are the temporal intensity distributions of the signal pulse and the known reference pulse, respectively, and τ is the time delay between the overlapping signal and reference pulses. Thus, by knowing the function $G^{(2)}(\tau)$ and the temporal intensity distribution of the reference pulse I_2, the temporal intensity profile of the studied signal pulse I_1 can be determined. It is important to note that this measurement method does not provide any information regarding the pulse phase and frequency modulation (chirp).

In general, when measuring the parameters of ultrashort pulses, the signal pulse under investigation is typically used as its own reference. In this case, the intensity distributions of the signal and reference pulses are identical (I_1=$I_2 = I$), and the second-order intensity autocorrelation can be described as follows:

$$A^{(2)} = \int_{-\infty}^{\infty} I(t) I(t-\tau) dt \quad (11)$$

The resulting function is always symmetric, with its maximum located at $\tau = 0$. Therefore, the primary drawback of this method is that the measurement provides no information regarding the asymmetry of the pulse. However, the technique remains widely used for the qualitative diagnostics of the temporal profile. Representative autocorrelation functions for different incident pulse intensity profiles are presented in Fig. 1.

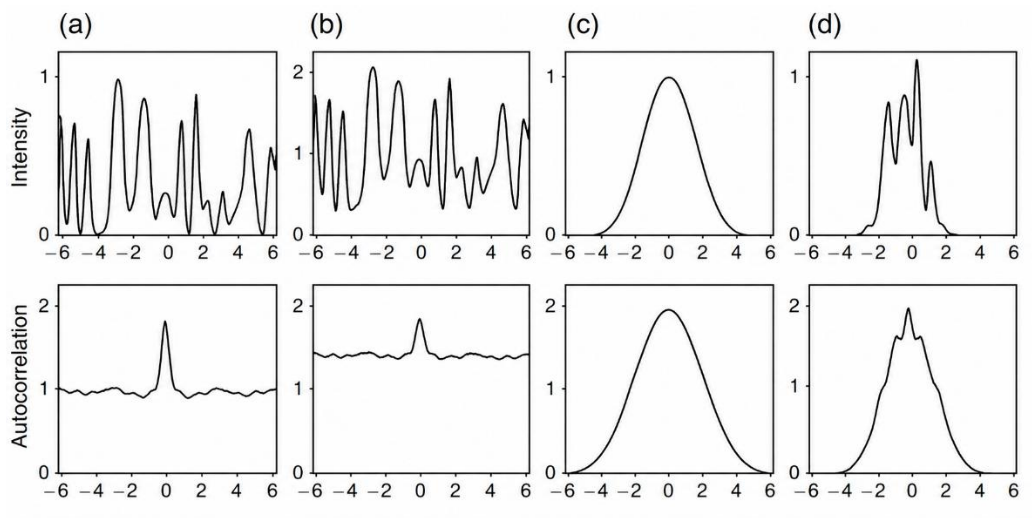

Fig. 1. Pulse temporal intensity distribution (top) and corresponding second-order autocorrelation functions (bottom). Adapted from [53].

Intensity autocorrelation is frequently used to determine the duration of an unknown pulse. However, in this case, an assumption must be made regarding the shape of the pulse's intensity profile (e.g., Gaussian, sech^2, etc.). Under these circumstances, the width of the measured autocorrelation curve τ_{ACF} is related to the duration of the pulse under investigation τ_p through a specific proportionality factor, and the pulse duration is determined more accurately based on the chosen pulse shape. For example, assuming the pulse has a Gaussian profile, the actual duration is calculated as follows: $\tau_p = \tau_{ACF}/\sqrt{2}$.

For a more detailed temporal quality analysis, high-dynamic-range autocorrelators can be employed, which are capable of distinguishing intensity fluctuations, such as satellite pulses, that are 10^6 times or more smaller than the peak signal and located in the vicinity of the main pulse. Such autocorrelators are particularly important in the study of high-temporal-quality laser systems, where evaluation of ultrashort pulse contrast is critical.

However, in this work, a low-dynamic-range (~10^3) intensity autocorrelator (*pulseCheck NX*, APE) based on non-collinear SHG was used. In this configuration, the signal pulse is split into two beams that overlap at a cross-angle within a nonlinear crystal. The intensity of the generated second-harmonic signal (the value of the autocorrelation function) is proportional to the square of the product of the overlapping pulse intensities. By varying the time delay between the pulses and recording the strength of the second-harmonic signal, the intensity autocorrelation curve can be reconstructed. As this method does not provide information regarding the pulse phase or temporal asymmetry, it is used solely for the qualitative analysis of ultrashort pulses.

2.2. Pulse temporal contrast analysis using a third-order autocorrelator

Alternatively, TC measurements can be performed using a more sensitive method – a third-order correlation. When the signal is generated from the investigated pulse itself, the method is referred to as third-order autocorrelation. In this process, the correlation signal exhibits a cubic dependence on the pulse intensity. The signal is typically produced by correlating a replica of the pulse converted to the second harmonic with the remaining part of the fundamental harmonic. Mathematically, the third-order correlation function is defined as:

$$G^{(3)}(\tau) = \int_{-\infty}^{\infty} I(t)I^2(t-\tau)dt, \quad (12)$$

where $I(t)$ denotes the pulse intensity and τ represents the temporal delay. The probe $I^2(t-\tau)$, formed through SHG, possesses a significantly higher temporal contrast [54]. Consequently, the resulting correlation signal more accurately reflects the temporal intensity structure of the pulse under investigation. These properties make third-order correlation a standard technique for high-dynamic-range temporal contrast analysis in femtosecond laser systems.

In this work, TC was measured using a *Sequoia-1000* (Amplitude Technologies) third-order autocorrelator. By utilizing a photomultiplier tube (PMT) and neutral density filters, the system achieves a high dynamic range of up to 10^{-10}. As shown in the simplified optical scheme (Fig. 2), the input pulse is split into two branches. The first branch is used for SHG (515 nm) and is combined with a motorized delay line. The second branch carries the residual fundamental signal. These pulses are recombined non-collinearly in a second nonlinear crystal to generate a third-harmonic correlation signal (343 nm). The amplitude of this signal is recorded by the PMT, with filters used to extend the measurement across the full dynamic range.

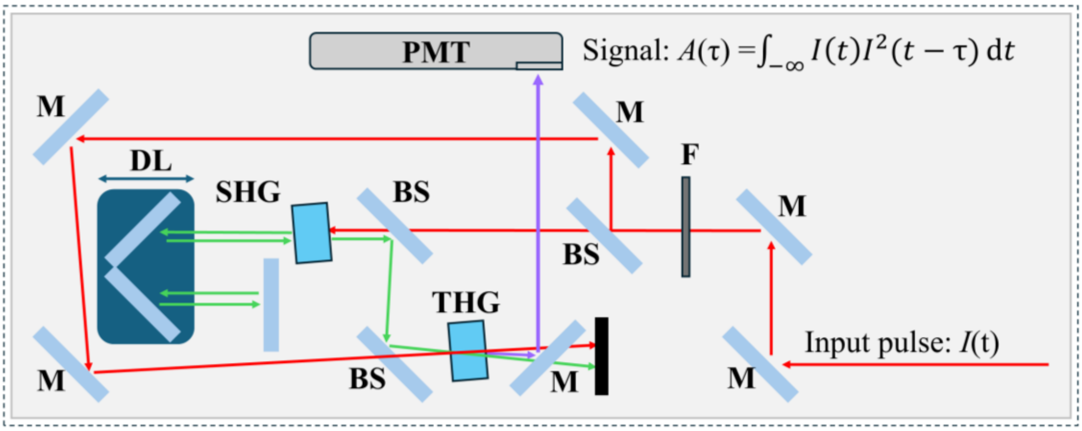

Fig. 2. Principal scheme of the third-order autocorrelator. Abbreviations: M – mirror, F – neutral density filter set, BS – beam splitter, DL – motorized delay line, SHG – second harmonic generation stage, THG – third harmonic generation stage, PMT – photo-multiplier tube detector.

2.3. Pulse envelope reconstruction using the FROG technique

While TC evaluation provided essential information regarding pulse cleanliness, a complete reconstruction of the pulse envelope requires a more comprehensive diagnostic approach. To achieve this, the frequency-resolved optical gating (FROG) method was employed. FROG is a well-established standard technique that allows for the characterization of an ultrashort pulse by retrieving its electric field and spectral phase. The method relies on recording a two-dimensional time-frequency spectrogram, from which the pulse structure is reconstructed using iterative algorithms. Unlike the intensity correlation, FROG identifies phase distortions, satellite structures, and asymmetric profiles. First described by R. Trebino and D. Kane [55,56], the mathematical form of the FROG trace is given by:

$$I_{(SHG-FROG)}(\omega,\tau) = \left|\int_{-\infty}^{+\infty} E(t,\tau) e^{(-i\omega t)} dt\right|^2, \tag{13}$$

where $I_{\text{SHG-FROG}}(\omega,\tau)$ represents the measured FROG trace – a two-dimensional intensity distribution as a function of frequency ω and time delay τ. The integral over time defines the Fourier transform of the field product, while its squared magnitude corresponds to the recorded second-harmonic signal intensity. In this way, the SHG-FROG trace reflects the inherent relationship between the temporal and spectral structures of the pulse.

The processing of the obtained FROG trace is performed using an iterative numerical algorithm, most commonly the generalized projections method. This algorithm relies on repeated transitions between the time and frequency domains using Fourier and inverse Fourier transforms.

The reconstruction procedure begins with an initial guess of the electric field $E(t)$, which can be chosen randomly or based on prior information about the pulse. From this guess, a theoretical FROG signal field is calculated, describing the correlation signal generated during the nonlinear process. Next, the signal field is transformed into the frequency domain, where its squared magnitude is compared with the experimentally measured FROG trace. The amplitude of the calculated signal is then replaced with the measured data, while the calculated phase is preserved. The modified signal field is returned to the time domain and constrained to satisfy the physical requirements of the nonlinear process (the SHG). Iterations continue until sufficient agreement between the theoretical and experimental traces is reached and the solution for the electric field $E(t)$ converges. The final remaining discrepancy is defined as the FROG error.

In this work, the two-dimensional time-frequency array was recorded using a custom-built FROG spectrometer (Ekspla), the principal layout of which is presented in Fig. 3. The recovery of the pulse envelope and spectrum via the iterative algorithm was performed using the commercial FROG software (Femtosoft Technologies).

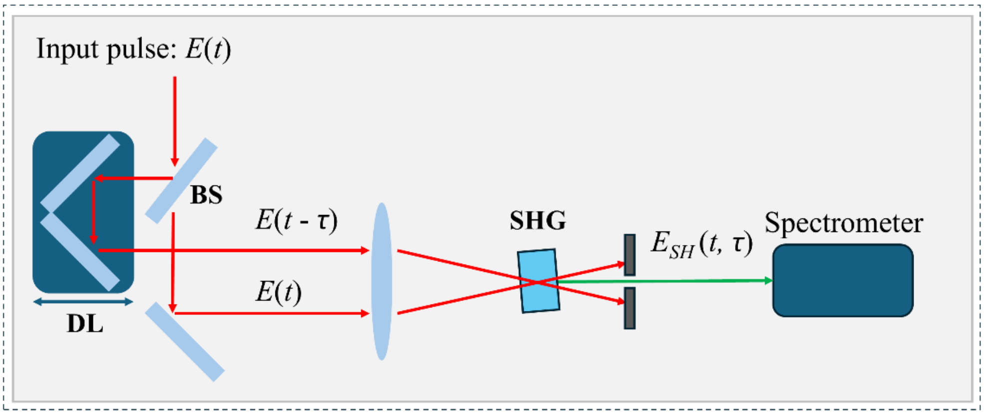

Fig. 3. Scheme of frequency-resolved optical gating measurement (FROG) based on second harmonic generation (SHG).

To complement the phase retrieval process, the specific dispersion characteristics of the pulse can be quantified through the retrieved spectral phase. Spectral phase derivatives, such as GDD and TOD, can be extracted by fitting a Taylor series polynomial (as in Eq. 3) of a desired order to the retrieved spectral phase data. This way, an approximate value of residual dispersion of the measured pulse, such as GDD or TOD, can be extracted. This approach will be implemented in Section 3.5 of the experimental results.

3. Results and Discussion

3.1. Temporal analysis of ultrashort pulses in a hybrid CPA system

To establish a baseline for the investigated parameters, the output pulse characteristics of the hybrid CPA laser *FemtoLux30* (Ekspla) were evaluated. The experimental setup is illustrated in Fig. 4, comprising the laser system and a third-order autocorrelator for temporal contrast analysis. The primary focus of this study was the CFBG pulse stretcher, highlighted by the red contour.

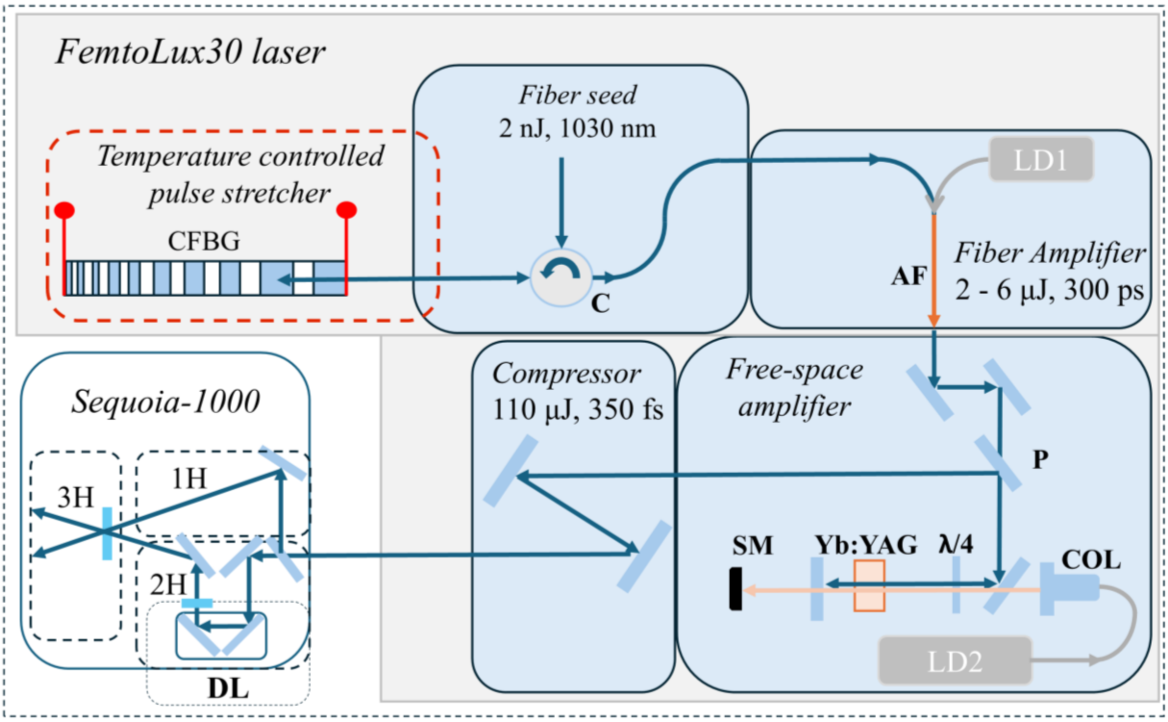

Fig. 4. Scheme of the investigated hybrid CPA laser *FemtoLux30* with the third-order autocorrelator *Sequoia-1000*, used for pulse temporal contrast analysis. Abbreviations: CFBG – chirped fiber Bragg grating, C – fiber circulator, AF – Yb-doped active fiber, P – polarizer, COL – pump beam collimator, SM – spherical mirror, DL – delay line, 1H/2H/3H – fundamental, second- and third-harmonic branches.

Initial seed pulses with 1030 nm central wavelength and picosecond duration were generated in a passively mode-locked fiber oscillator, based on Yb-doped active fiber and a semiconductor saturable-absorber mirror (SESAM) (Fig. 4, segment "Fiber seed"). Spectral shaping of the generated pulses was achieved via fiber amplification and subsequent nonlinear propagation in a passive fiber, resulting in spectral broadening primarily driven by SPM. After spectral broadening, a chirped fiber Bragg grating (CFBG) was used to stretch the pulse duration to approximately 400 ps (Fig. 4, segment "CFBG"). The CFBG pulse stretcher was placed in a temperature-controlled module, allowing a linear temperature gradient to be applied along the CFBG. The temperature-gradient-induced thermo-optic effect enabled active control of the second-order dispersion (GDD), corresponding to the linear chirp. The linearly chirped pulse was directed into a fiber amplifier, where it was amplified by a factor of approximately 10^3 from 2 nJ to 2–6 µJ pulse energy. Then the amplified pulse was directed into a free-space amplification stage with a Yb:YAG active medium, where it was further amplified in a double-pass configuration (Fig. 4, “Free-space amplifier” segment).

Finally, the dispersion of the amplified chirped pulse is compensated using a free-space pulse compressor based on a transmission diffraction grating (Fig. 4, segment “Compressor”). In the following sections, the output pulse energy from the free-space amplifier was varied within the range of 32–200 µJ to examine various pulse characteristics.

The output pulse quality was first characterized at a seed pulse energy of 4.5 µJ and a subsequent amplification to 110 µJ in the free-space amplifier. The pulse spectrum and duration measured using a second-order (intensity) autocorrelator *PulseCheck NX* (APE) are presented in Fig. 5. The measured autocorrelation function (Fig. 5(A)) yielded an output pulse duration of 351 fs (full width at half maximum (FWHM)), while the corresponding optical spectrum (Fig. 5(B)) indicated a bandwidth of around 3.2 nm (FWHM).

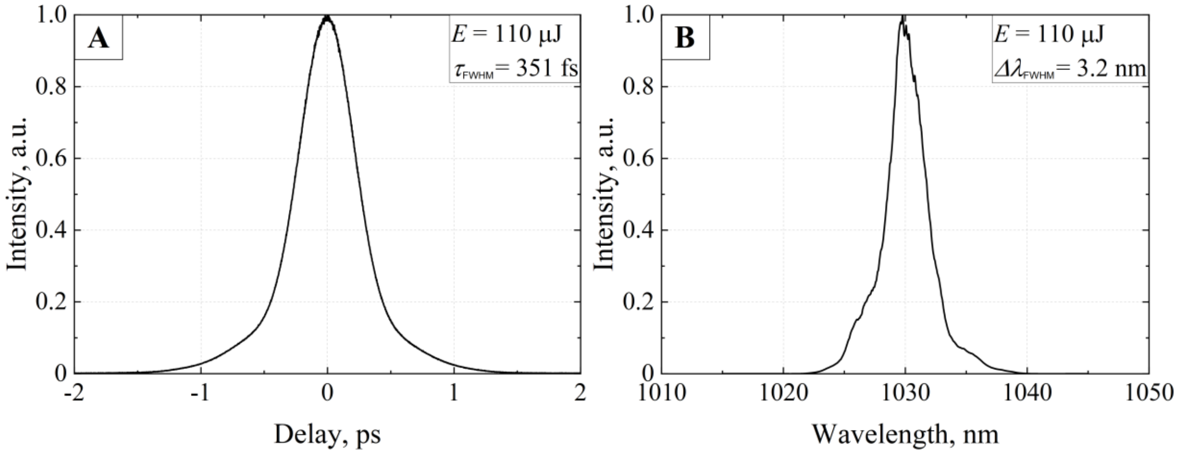

Fig. 5. (A) Autocorrelation trace and (B) spectrum of pulses generated by the investigated hybrid CPA system operating at 110 µJ pulse energy.

Subsequently, temporal contrast (TC) measurements were performed using a third-order autocorrelator. The resulting autocorrelation signal was used to evaluate temporal pulse quality, specifically comparing the peak intensity to the pulse periphery. In the following sections, TC is defined as the intensity ratio between the main pulse peak and the highest intensity satellite pulse.

The measured third-order autocorrelation trace over a delay range of ±100 ps is presented in Fig. 6. Based on the ratio of the main pulse and the highest-amplitude satellite signal, the TC was determined to be $5.5 \cdot 10^{-4}$. On the other hand, the background intensity level within the ±100 ps temporal window was on the order of 10^{-5} to 10^{-6}. As discussed in Section 1.2.3, this incoherent background is primarily attributed to the ASE accumulated in the fiber amplifier.

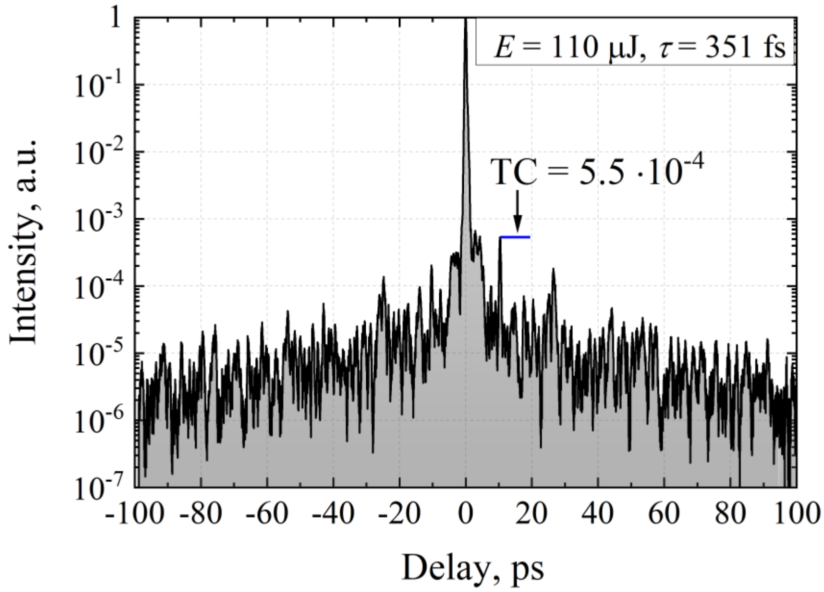

Fig. 6. Third-order autocorrelation trace of a 110 μJ output pulse from the *FemtoLux30* laser, measured over a ±100 ps delay range. Pulse temporal contrast (TC) was calculated as the intensity ratio of the main peak and the satellite pulse at approximately 10 ps delay.

The reliability of the TC measurement was assessed through additional experiments, in which the linear response and dynamic range of the third-order autocorrelator were verified. To begin with, the linearity of the correlation signal was evaluated using an artificially generated satellite pulse of a known intensity. The satellite pulse was introduced by inserting an uncoated 6 mm-thick UV-fused silica (UVFS) plate into the optical path at a small angle (<1°). Partial reflections at optical interfaces produced a delayed pulse replica with a well-defined intensity. The temporal delay of the satellite pulse was estimated from the round-trip propagation inside the UVFS plate using the plate thickness d and refractive index $n_g \approx 1.45$, yielding a delay of approximately 58 ps. In addition, the theoretical satellite pulse intensity was estimated using

Fresnel coefficients, as it can be approximated by R^2T, corresponding to two internal reflections and one transmission through the rear surface:

$$I_{\text{sattelite}} = I_0 \cdot R^2 \cdot T; \quad R = \left((n_1 - n_2)/(n_1 + n_2)\right)^2. \tag{14}$$

In the measured autocorrelation trace (Fig. 7(A)), a mismatch between the calculated and measured satellite pulse intensity was estimated to be around 1.5, which is therefore attributed to the systematic measurement error of the autocorrelator.

Furthermore, the dynamic range of the autocorrelator was evaluated by alternately blocking the fundamental-harmonic (FH) branch or second-harmonic (SH) branch within the device (Fig. 7(B), FH/SH branch). Blocking either beam branch inside the autocorrelator suppresses third-harmonic generation, resulting in the signal originating from the background noise. The experiment confirmed a dynamic range of approximately 10^{-10}, demonstrating that the chosen instrument had sufficient sensitivity to resolve low-intensity features near the main pulse peak.

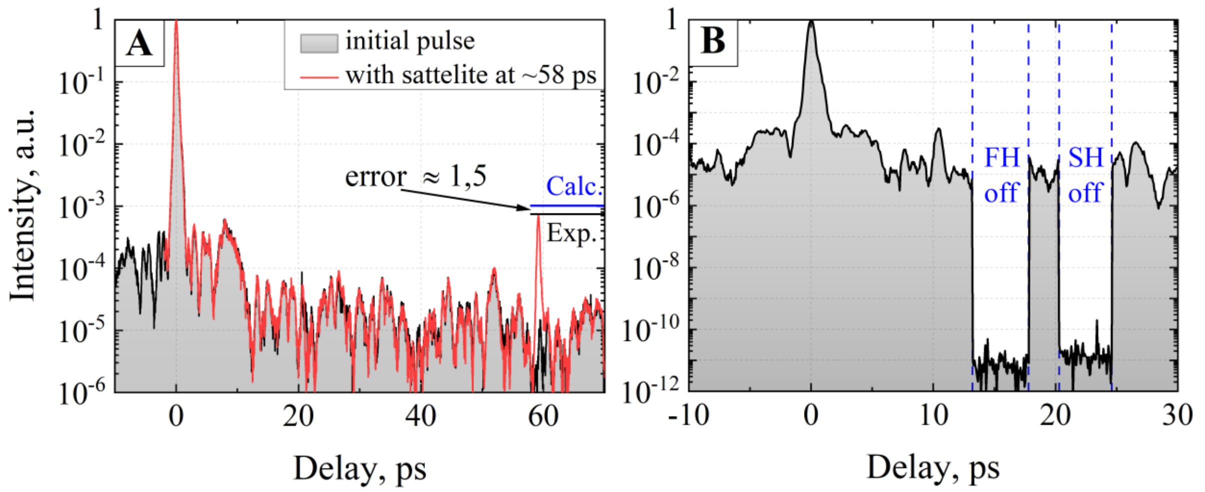

Fig. 7. (A) Third-order autocorrelation trace of a pulse with an artificially generated satellite due to double reflection in a UVFS plate, and (B) third-order autocorrelation obtained when either the FH or the SH branch is blocked inside the autocorrelator.

3.1.1. Impact of fiber amplifier on temporal contrast

In this section, the temporal quality of the output pulse was compared for different pulse energy levels in the fiber seed source. Third-order autocorrelation measurements for seed pulse energies of 2 μJ and 6 μJ are presented in Fig. 8. The traces indicate that increasing the seed pulse energy by a factor of three (to 6 μJ) results in a degradation of the TC by approximately 5 times. Additionally, a main pulse energy ratio was evaluated. This metric was defined as a ratio of the main pulse energy, integrated within a ±1 ps interval (Fig. 8, blue regions), and the total energy, integrated over a chosen temporal window (±30 ps). The constructed pulse energy ratio $E_{\pm 1\text{ps}}/E_{\pm 30\text{ps}}$ revealed that the energy contained in the main peak decreased from 99.4% to 97.9%, as the pulse energy from the fiber amplifier output was tripled.

The reduction in the main pulse energy content can be attributed to increased ASE and pulse distortions arising from nonlinear phase accumulation in the fiber amplifier. The B-integral (denoted B in Fig. 8) was calculated using a FCPA modelling platform developed by R. Danilevičius and T. Bartulevičius. The estimated B-integral indicates that a 2.7 times larger accumulated nonlinear phase results in a degradation of temporal contrast by a factor of 5.

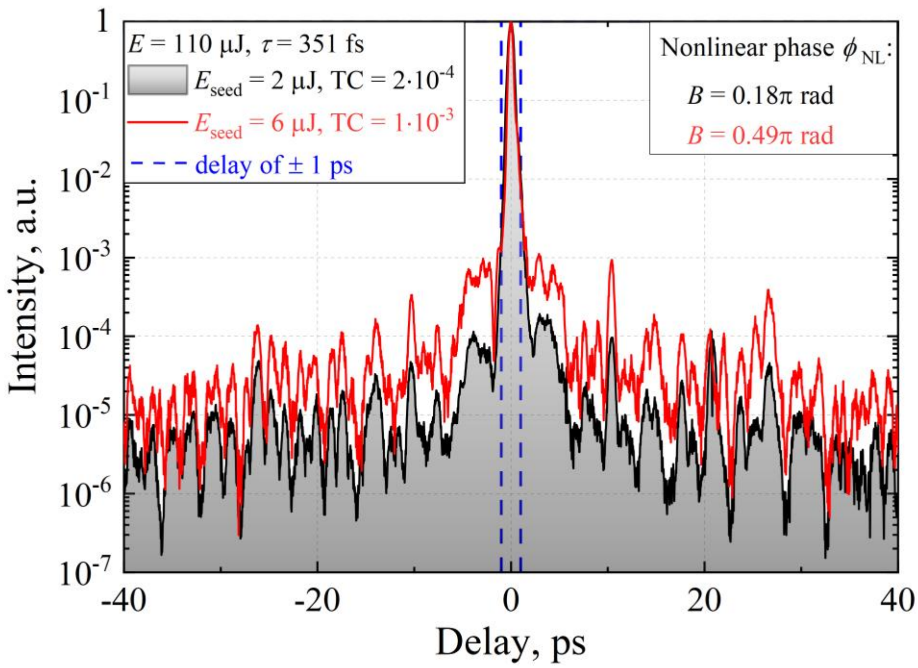

Fig. 8. Third-order autocorrelation traces for the output pulses, when the seed pulse was amplified to 2 μJ (black) and 6 μJ (red) in the fiber amplifier stage. The nonlinear phase shift inside the fiber amplifier was estimated using the B-integral (9). Delay of 1 ps, used for main peak energy analysis, is marked in blue.

3.2. Numerical simulation: impact of CFBG spectral amplitude and group delay ripples on compressed pulse temporal quality

This section presents numerical modelling performed to evaluate the impact of a CFBG pulse stretcher quality on the compressed pulse. Using the earlier introduced FCPA model, the quality of the compressed pulse was analyzed in relation to spectral amplitude and GD distortions introduced in a CFBG pulse stretcher.

The representative spectral reflectivity and GD ripples of the reference pulse stretcher are presented in Fig. 9. The reflection and GD profiles correspond to a standard CFBG used as the baseline component in the investigated FCPA system. To investigate the modelled pulse sensitivity to increased phase noise, an additional GD ripple profile (Fig. 9(B), red curve) was generated by tripling the amplitude of the measured reference GD ripples.

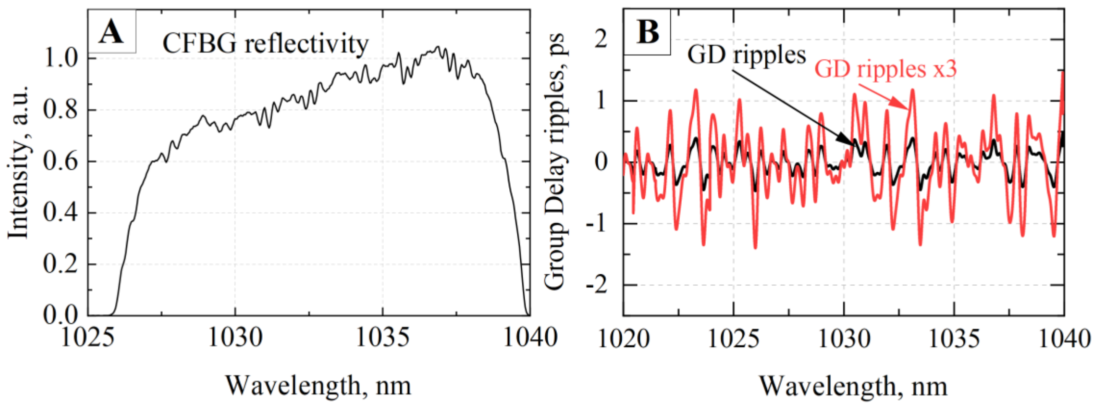

Fig. 9. (A) Modelled CFBG reflectivity and (B) group delay (GD) ripples of the reference CFBG. The triple amplitude GD ripple profile (B, red curve) was used to assess the impact of higher-magnitude distortions.

The distortions from Fig. 9 were integrated into the FCPA model's pulse stretching stage to represent the transfer function of a non-ideal CFBG. Following the application of a linear chirp and the corresponding spectral and GD distortions, the pulse was amplified to approximately 1 μJ inside a YDF amplifier model. To ensure that the resulting temporal distortions were dominated by the CFBG impact rather than nonlinear effects, the B-integral of the amplification stage was maintained well below 1π rad. Finally, the simulated pulse was compressed using a linear chirp of opposite sign, resulting in a compressed pulse duration of around 317 fs.

Figure 10(A, B) presents the resulting temporal and spectral intensity profiles of a compressed pulse for three distinct pulse stretching conditions: an ideal case with no distortions, the application of measured reference spectrum and GD ripples, and the synthetic profile with tripled GD ripple amplitude. The introduction of distortions led to a clear degradation of pulse temporal contrast, characterized by an increased pedestal and the appearance of satellite features near the main peak, alongside a corresponding modulation of the output spectrum. Notably, the application of triple-amplitude GD ripples (Fig. 10, red curve) led to an order-of-magnitude increase in the intensity of the temporal satellite features. In this case, the degradation of pulse quality was clearly visible even on a linear scale, as shown in the inset of Fig. 10(C).

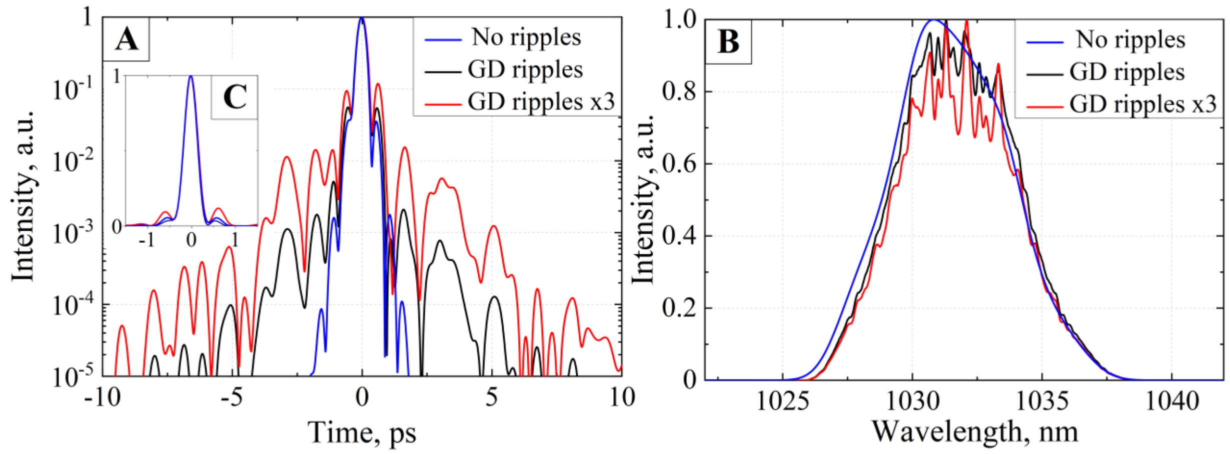

Fig. 10. (A) Simulated compressed pulse from the FCPA model and (B) the corresponding spectrum for three scenarios: pulse stretching with no distortion (blue curve), reference spectrum and GD ripples (black curve), and spectrum ripples with threefold amplitude GD ripples (red curve). Inset (C) presents the compressed pulse on a linear scale.

Subsequently, a higher inscription quality CFBG was introduced. The new component, characterized by significantly smoother spectral reflectivity and GD profiles, is investigated in the following simulation and further experimental sections. The representative spectral reflectivity and GD ripple profiles for the high-quality stretcher (abbreviated $CFBG_{high\text{-}Q}$), and the reference component ($CFBG_{ref}$) are compared in Fig. 11. Quantitatively, the high-quality component, compared to the reference, exhibited a substantial reduction in root mean square (RMS) amplitudes for both spectral reflectivity (1% vs. 2.5%) and GD ripples (0.08 ps vs. 0.22 ps).

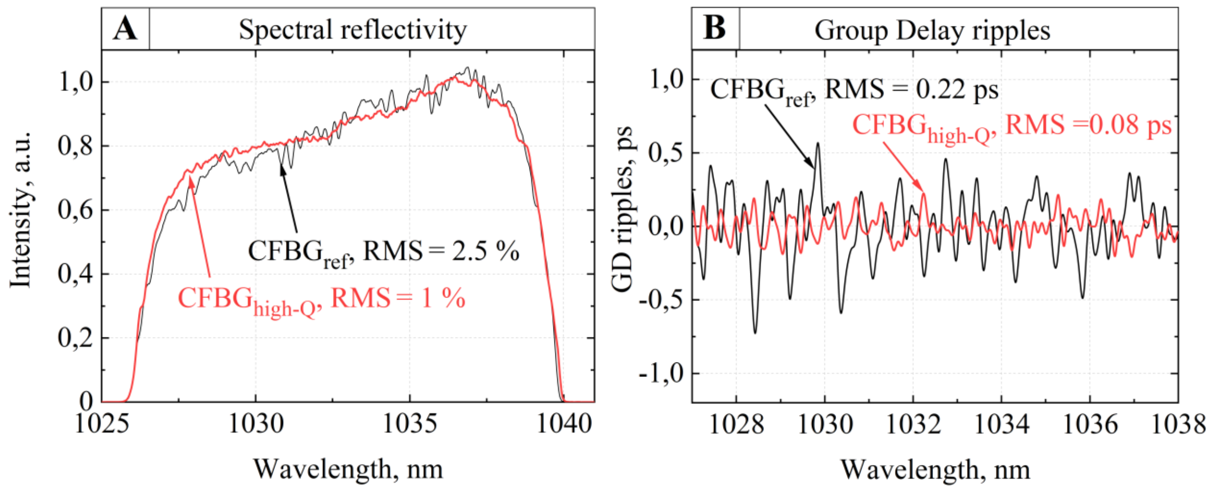

Fig. 11. (A) Normalized reflectivity profile and (B) group delay (GD) ripples from the target value for a typical reference stretcher $CFBG_{ref}$ and high inscription quality stretcher $CFBG_{high\text{-}Q}$.

A comparison of the compressed pulses, generated by incorporating different CFBG spectral and GD ripple profiles from Fig. 11 into the FCPA model, is presented in Fig. 12. The introduction of the high-quality pulse stretcher resulted in a notable improvement in pulse quality, as satellite features in discrete temporal regions (> 3 ps delay range) were effectively diminished. The suppression of time-domain noise directly correlated with lower RMS spectral reflectivity and GD ripples of the $CFBG_{high\text{-}Q}$ pulse stretcher, as other pulse parameters of the modelled FCPA system were kept constant.

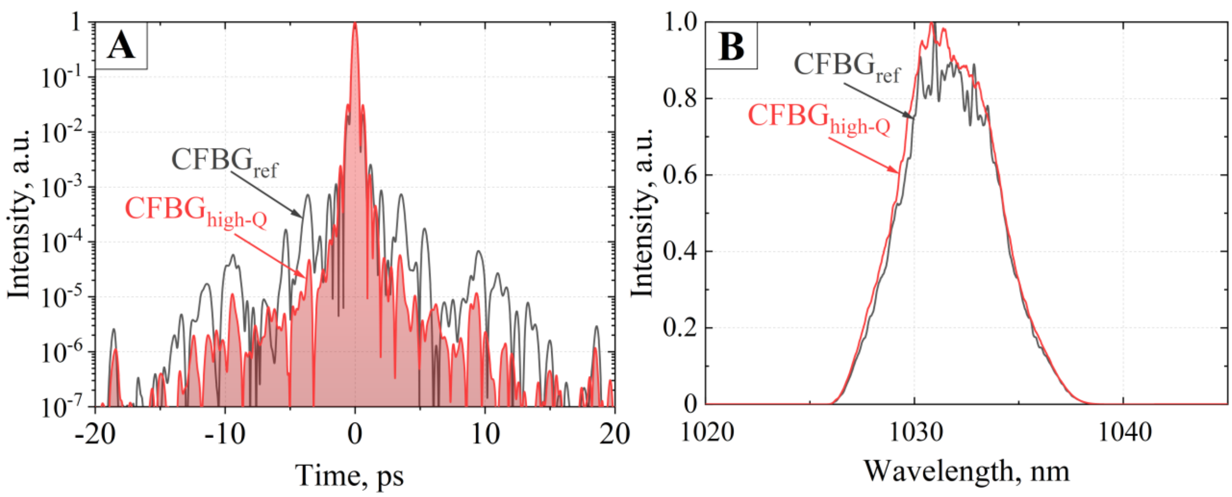

Fig. 12. (A) Simulated temporal profile of a compressed pulse together with its spectrum (B), when corresponding spectral and GD distortions for reference ($CFBG_{ref}$) and high-quality ($CFBG_{high\text{-}Q}$) components are added during the pulse stretching stage.

As demonstrated in the FCPA simulations (Fig. 10 and Fig. 12), spectral reflectivity and GD distortions during the stretching stage significantly degrade the compressed pulse quality. Therefore, application of a higher-quality CFBG is expected to provide a measurable improvement in the output pulse quality of the investigated experimental hybrid CPA system.

3.3. Temporal contrast improvement using a higher-quality CFBG

The following section provides experimental analysis of the presented high-quality CFBG impact on the output pulse quality of a hybrid CPA system. Third-order autocorrelation measurements were performed to evaluate the output pulse quality when the reference CFBG inside the fiber seed source was replaced with two high-quality stretchers: $\mathrm{CFBG}^{1}_{high-Q}$ and $\mathrm{CFBG}^{2}_{high-Q}$ (Fig. 13(A,B)). Based on the satellite pulse at a delay of 10 ps, the introduction of higher-quality CFBGs increased the output pulse TC up to 3 times, whereas the background level, further from the main peak, remained largely unchanged.

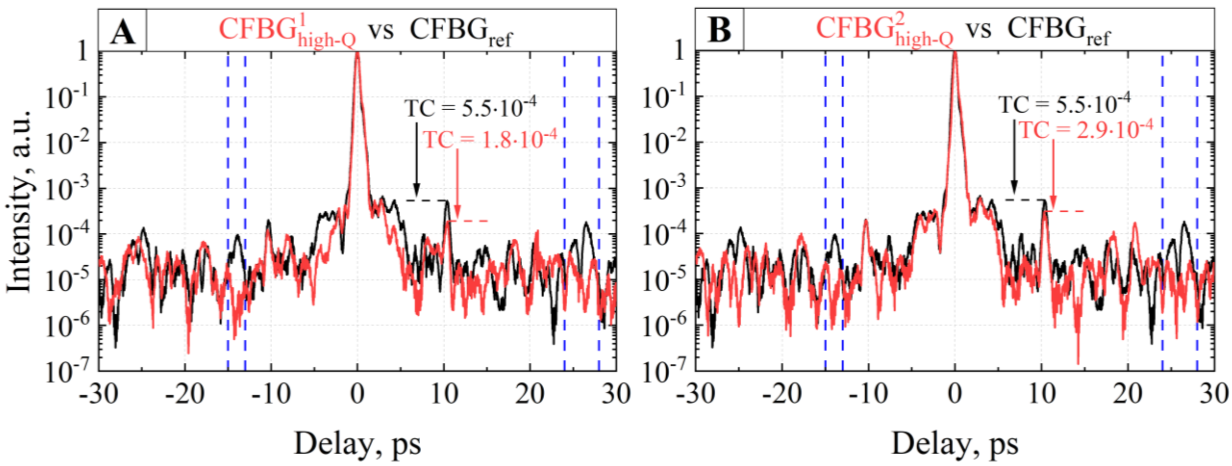

Fig. 13. A comparison of third-order autocorrelation functions of a reference pulse stretcher (CFBG_{ref}) and two high-quality CFBG components ($\mathrm{CFBG}_{high\text{-}Q}$), depicted in (A) and (B) graphs. Blue contours indicate delay regions where temporal intensity structures have effectively vanished.

The 10 ps satellite, used for TC estimation, was likely caused by parasitic reflections in the fiber seed source, as its temporal position remains unchanged in both CFBG traces. In contrast, the temporal intensity structures observed at delays of −15 ps and +25 ps (marked in blue in Fig. 13) may be attributed to distortions introduced by the CFBG, since these peaks are absent in both experiments when higher-quality CFBGs were employed.

Following, a main pulse energy ratio was evaluated using the third-order autocorrelation measurements at a seed pulse energy of 6 μJ. The main pulse energy fraction within the ±30 ps delay window increased from 97.9% to 98.6% when the high-quality CFBG was introduced. Accordingly, the energy in the background decreased from 2.1% to 1.4% (approximately a factor of 1.5). While the background energy was suppressed notably (1.5 times), the effect on the total energy integral remained minimal due to the inherently low intensity of the pulse pedestal.

Additionally, figure 13(A) shows a localized TC improvement within the ±8 ps delay that is absent using the other high-quality CFBG in Fig. 13(B). This effect may stem from a nonuniform CFBG quality or accidental compensation of higher-order dispersion. To isolate the dispersion changes introduced by the CFBGs, the pulse compressor was kept fixed throughout the experiments. While this facilitates a direct comparison of the CFBGs, inherent variations in their GDD and TOD parameters inevitably result in different compression outcomes upon interchange.

3.4. External post-compression and impact of a higher-quality CFBG on sub-60 fs pulses

In this part of the study, the output pulse duration from the *FemtoLux30* laser was reduced using *Yabby* (Lastek) external post–compression module (Fig. 14). In accordance with the principles outlined in Section 1.3, the investigated post-compression approach utilizes a multi-pass cell with a fused silica plate to induce nonlinear spectral broadening, followed by dispersion compensation with chirped mirrors. As the spectral broadening redistributes seed-induced spectral and GD ripples across a wider spectral bandwidth, the method may effectively magnify the impact of CFBG-induced distortions. Therefore, the use of different-quality CFBG pulse stretchers is expected to yield a more significant change in TC of the post-compressed pulse.

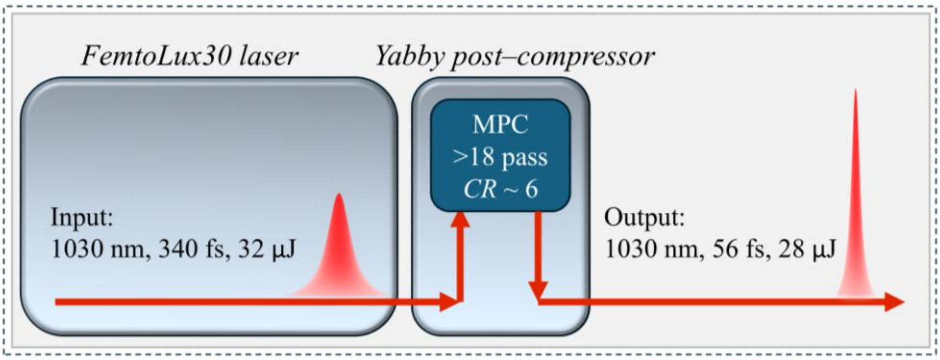

Fig. 14. Block diagram of the hybrid CPA system (*FemtoLux30*) combined with an external post-compression module (*Yabby*), providing a pulse compression ratio (CR) of 6.

Optimal post-compression with the given setup was achieved for pulses with 32 μJ energy and a CPA output pulse duration of 340 fs. The total energy transmission through the post-compression module was approximately 88%.

The compressed pulse envelope was reconstructed using the FROG method with a retrieval error of approximately 0.3%. The FROG-analysis-retrieved pulse envelope (Fig. 15(A)) demonstrates that the incident 340 fs pulse was compressed by a factor of approximately 6, resulting in a duration of 56 fs. Furthermore, low-intensity temporal structures emerged in the vicinity of the main pulse and remained observable even on a linear intensity scale. These intensity fluctuations, commonly referred to as pulse wings, arise from incomplete compensation of higher-order dispersion terms and residual distortions in the pulse spectral amplitude and phase.

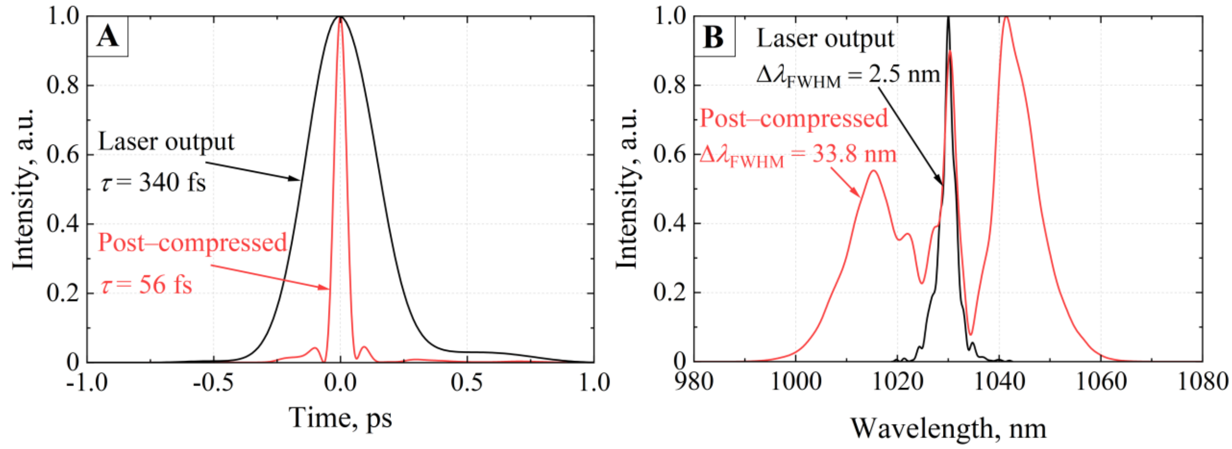

Fig. 15. Temporal and spectral characterization of the pulse based on FROG measurements. (A) Retrieved temporal intensity profiles before and after post-compression. (B) Corresponding spectral intensity distributions. The FROG retrieval error was < 0.1%.

The retrieved pulse spectrum in Fig. 15(B) reveals a significant spectral broadening in the applied post-compression module. The pulse bandwidth increased significantly, from 2.5 nm (FWHM) to approximately 33.8 nm (FWHM). However, due to the double-peaked spectral structure, the FWHM bandwidth of the post-compressed pulse is not fully representative and is therefore provided for reference only.

Subsequently, third-order autocorrelation measurements were performed to assess the variations in the TC of the externally compressed pulse relative to the initial pulse quality (Fig. 16(A)). More pronounced low-intensity temporal structures are observed in the periphery of the externally compressed pulse (Fig. 16(A), delay range from −2 ps to 3 ps), which are likely associated with residual uncompensated higher-order dispersion. Additionally, it is evident that after post-compression, the intensity pedestal near the main peak is significantly reduced, resulting in a locally increased TC by approximately 5.8 times. The enhanced TC after post-compression can be attributed to selective nonlinear spectral broadening and subsequent spectral phase compensation, which primarily affects only the high-intensity region of the pulse (the main peak). Consequently, the observed TC enhancement is intrinsically linked to the pulse compression ratio (CR) of approximately 6.

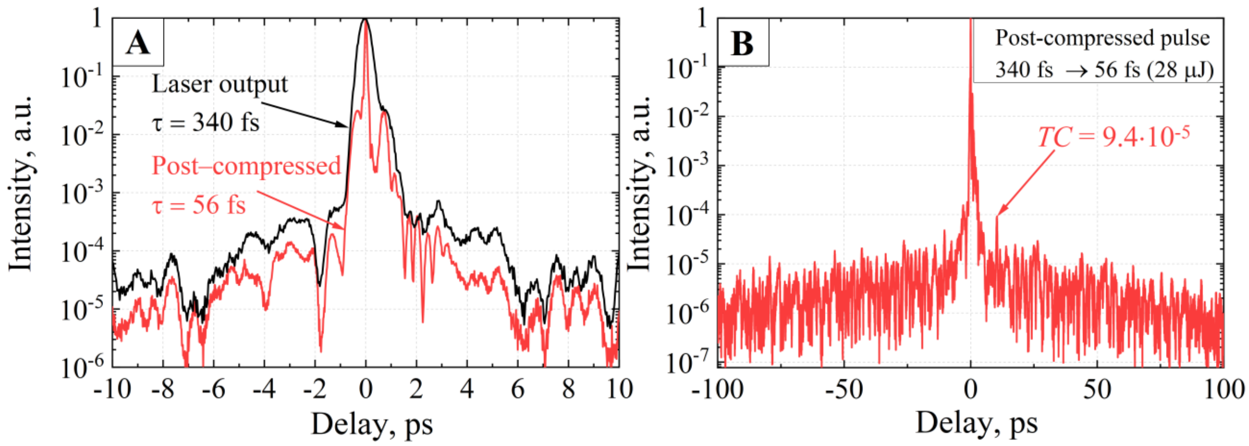

Fig. 16. (A) Third-order autocorrelation traces of the pulse before (340 fs) and after external post-compression to 56 fs; (B) post-compressed pulse trace with indicated temporal contrast value (TC).

Additionally, the TC of the 56 fs pulse was characterized using third-order autocorrelation over an extended ±100 ps delay window (Fig. 16(B)). Based on the most prominent satellite feature at a delay of 10 ps, the contrast was determined to be $9.4\cdot10^{-5}$. Notably, no additional higher intensity temporal satellites were induced by the post-compression process

In the next stage, the impact of CFBG quality on the post-compressed pulse was evaluated. The reference CFBG in the seed source was replaced with the higher-quality variant, and third-order autocorrelation measurements were performed (Fig. 17(A)). The calculated pulse energy ratio $E_{\pm200\mathrm{fs}}/E_{\pm10\mathrm{ps}}$, with the main pulse defined within a ±200 fs delay range and normalized to the full measurement window (±10 ps), shows that the energy contained in the main peak increased from 93.2% to 96.5% when the high-quality CFBG was used.

The relative change in background energy of the post-compressed pulse was more pronounced than for the output pulse in Section 3.2, yielding a reduction factor of 2 compared to the previous 1.5. The results indicate that the spectrally broadened pulse becomes more sensitive to seed-induced distortions, leading to more pronounced temporal distortions after compression.

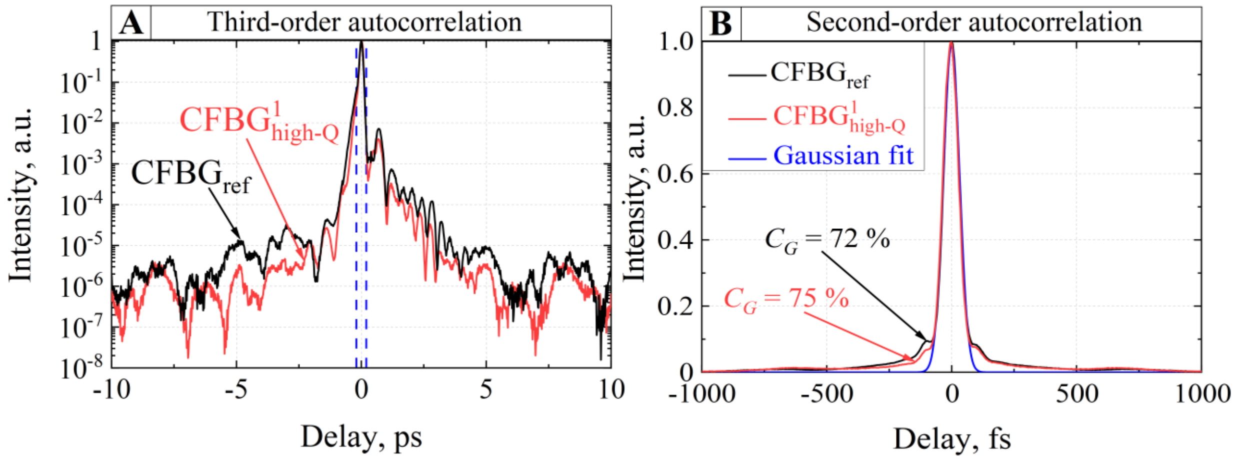

Fig. 17. Third-order (A) and second-order (B) autocorrelation traces of the post-compressed pulse (~56 fs, 28 μJ) for the reference CFBG (CFBG$_{ref}$) and the high-quality stretcher (CFBG$_{high-Q}$). The ±200 fs delay range used to estimate the main pulse energy fraction in (A) is indicated by dashed blue lines. The temporal pulse quality in (B) is quantified by the Gaussian contrast parameter C_G, which represents the overlap between the autocorrelation function and its Gaussian fit.

The post-compressed pulse quality using different CFBGs was alternatively analysed on a linear scale using second-order autocorrelation (Fig. 17(B)). The change was quantified using a new metric for pulse quality – a Gaussian correlation (C_G) – defined as the ratio of integrals of a Gaussian approximation and the measured autocorrelation function. It was estimated that the Gaussian correlation increases from 72% to 75%, further validating the improvement through a secondary measurement method.

Additionally, the FROG-retrieved pulses for different CFBGs used in the seed source are shown in Fig. 18. The results indicate that the amplitude of a temporal pulse wing, visible at a delay of around -110 fs, was reduced by a factor of 2. However, the observed reduction in this temporal feature may be attributed to accidental dispersion compensation rather than intrinsic CFBG quality, a possibility discussed at the conclusion of Section 3.3.

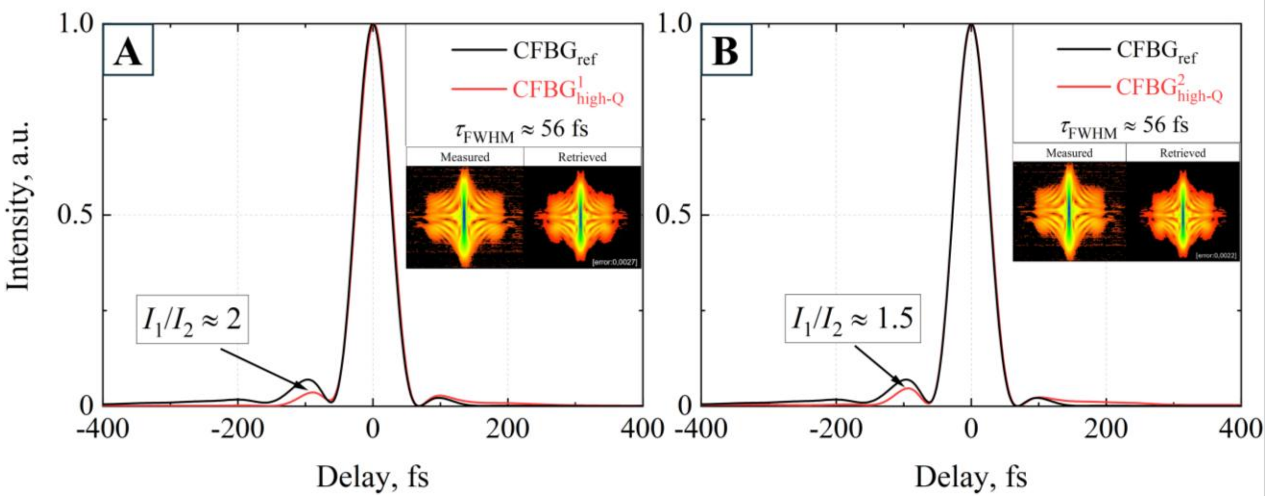

Fig. 18 Temporal pulse envelopes retrieved via FROG analysis for the reference CFBG (black) and higher-quality variants (red) incorporated into the seed source. Panels (A) and (B) correspond to the two investigated higher-quality pulse stretchers.

3.5. Investigation of temporal contrast enhancement via Kerr lens filtering

In this chapter, an external temporal contrast enhancement (CE) setup was implemented at the laser output. The investigated scheme is based on Kerr-lens filtering methodology, as described in section 1.2.4. This part of the study aims to validate the proposed temporal CE method using an optical arrangement comprising focusing optics, a few-millimeter-thick Kerr plate, and a 100 μm-diameter spatial filtering aperture (Fig. 19).

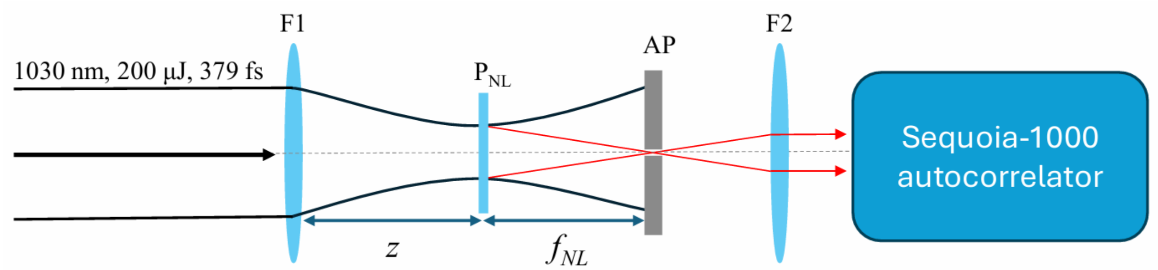

Fig. 19. Optical scheme of Kerr lens filtering. Abbreviations: F1 – focusing lens (f = 400 mm), P_{NL} – nonlinear plate, z – position of the plate, f_{NL} – nonlinear focal length, AP – filtering aperture (D = 100 μm), F2 – collimating lens (f = 110 mm).

Initially, the laser system was set to operate at 200 μJ pulse energy and a compressed pulse duration of 379 fs. The collimated beam from the laser was then focused using a plano-convex lens with a focal length of 400 mm. To induce the required nonlinear phase shift, the Kerr medium, a 0.7 mm BK7 plate or a 3 mm UVFS substrate, was positioned near the beam waist. The incident intensity at the nonlinear plate P_{NL} was tuned by moving the plate longitudinally to induce a desired

Kerr lens. In particular, the beam diameter ratio of the self-focused pulse peak (Fig. 19, shown in red) and that of the linear background (dark curve) was maximized. This enabled maximum spatial discrimination of the peak pulse at the filtering aperture AP, located at the plane of nonlinear focus f_{NL}. Finally, the output beam was collimated using an additional lens (f = 110 mm) and directed towards the third-order autocorrelator for TC measurements.

The temporal CE method was initially modelled by evaluating the Kerr-lens focusing and the spatial filtering. Firstly, the input pulse intensity profile was reconstructed using the FROG technique. Then, the nonlinear focal length (Kerr focal length) was calculated for each temporal slice of the pulse based on its instantaneous intensity profile (Fig. 20(A)). The calculated focal lengths for each temporal slice were approximated as thin lenses and incorporated into beam propagation simulations using the *reZonator* software (Orion-project), which is based on the ABCD matrix method. The simulated beam profiles for all temporal slices were subsequently combined at the aperture plane by considering their relative energy weighting. This way, the spatial distribution of the Kerr-lensed pulse was reconstructed (Fig. 20(B)). As shown in the figure by the red dashed lines, a small aperture shall be placed at this plane to selectively transmit the strongly self-focused central portion of the beam while blocking the unfocused low-intensity temporal structures. Therefore, an improved TC of the pulse peak versus the pulse periphery is expected.

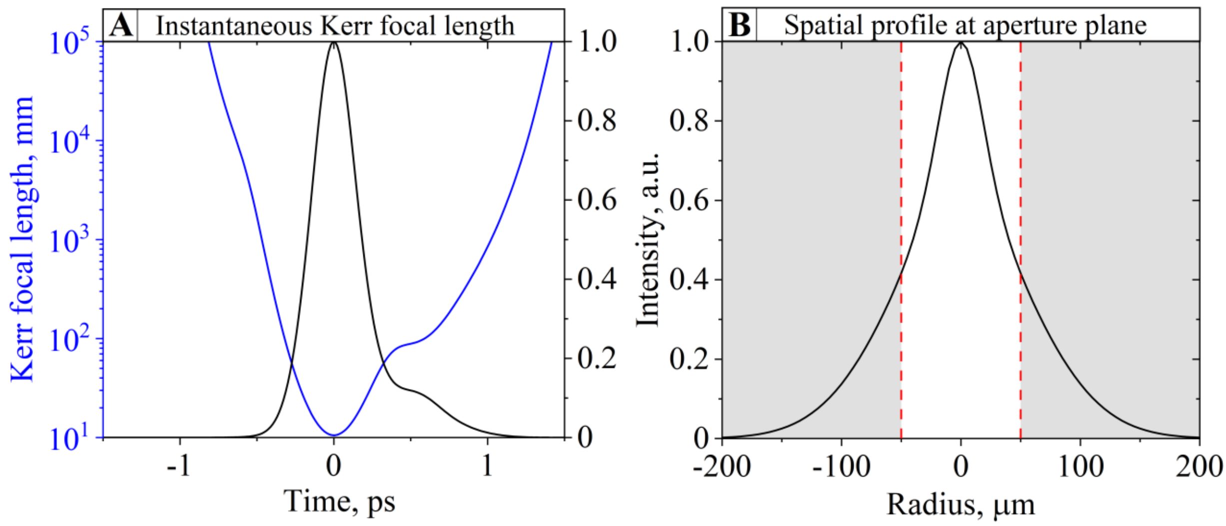

Fig. 20. Estimated Kerr focal length together with the normalized instantaneous pulse power (A), and integrated spatial profile of the Kerr-lensed pulse at the aperture plane (B). The red contours indicate the 100 μm diameter aperture.

An experiment was conducted to validate the proposed temporal CE approach. The setup consisted of a 200 μJ input laser pulse, a focusing lens (f = 400 mm), a 0.7 mm BK7 glass plate used as a Kerr medium, and a 100 μm diameter aperture used for spatial filtering. The calculated nonlinear phase shift for the pulse in this optical layout resulted in a B-integral of 2.08 rad. Figure 21 shows the third-order autocorrelation traces before and after Kerr-lens filtering, indicating a reduced intensity in the pulse periphery. In this case, it resulted in a mild temporal CE of 2 times. On the other hand, the satellite pulse at a delay of 7 ps did not decrease in amplitude. This pulse originates from a double reflection in the 0.7 mm BK7 plate and represents a satellite of an already Kerr-lensed input pulse. Consequently, its spatial propagation was equivalent to that of the main pulse peak, and it was therefore not filtered by the fixed aperture. The physically accurate representation of this satellite pulse validates the third-order autocorrelation analysis used to compare the TC changes discussed in this section.

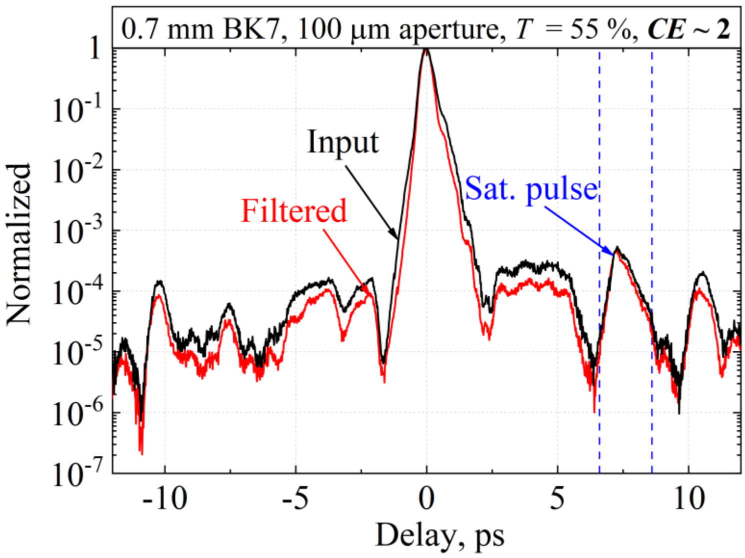

Fig. 21. Third-order autocorrelation traces before and after Kerr-lens filtering using a 0.7 mm BK7 plate and a 100 μm diameter aperture, yielding a transmission of 55% at an input pulse energy of 200 μJ. Blue color indicates the double-reflection satellite pulse from the BK7 plate.

Further, the temporal CE scheme was reconfigured to achieve a larger B-integral of approximately 3.55 rad, resulting in stronger self-focusing of the peak pulse. Accordingly, a 3 mm UVFS plate was used as the Kerr medium, while the remaining components were left unchanged. The third-order autocorrelation traces for input and output (filtered) pulses are presented in Fig. 22.

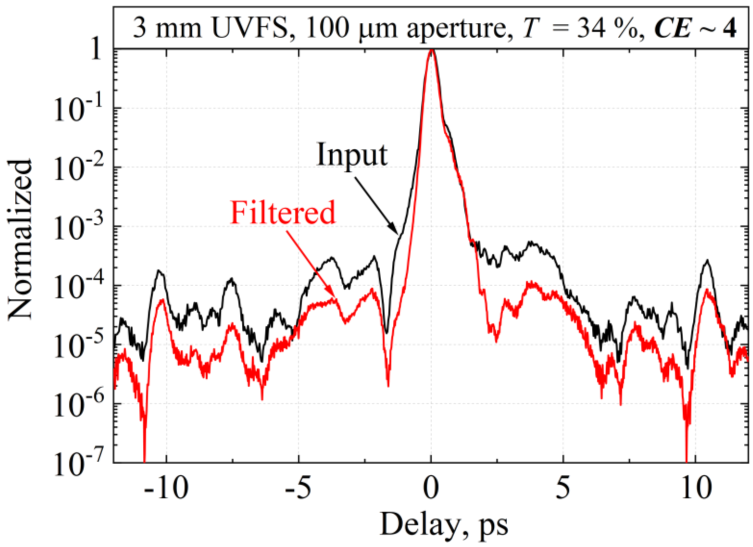

Fig. 22. Third-order autocorrelation traces before and after Kerr-lens filtering using a 3 mm UVFS plate and a 100 μm diameter aperture, yielding a transmission of 34 % at an input pulse energy of 200 μJ.

The application of stronger Kerr lensing resulted in more effective filtering of the pulse periphery, with an estimated temporal CE factor of 4. However, compared to the previous case, the overall energy transmission decreased significantly, from 55% to 34%. These measurements for temporal CE reveal a clear trade-off of this method, as further improvement of TC would require even stronger Kerr lensing, corresponding to a sufficiently larger B-integral. Alternatively, a more aggressive spatial truncation using a smaller-diameter aperture could be used; however, at the cost of higher transmission losses.

Following, an analysis of the filtered and incident pulse quality was performed to evaluate the resulting pulse after the investigated Kerr-lens filtering scheme. The pulse spectra before and after Kerr-lens filtering were measured (Fig. 23(A)). The results indicate strong SPM, leading to spectral broadening and the formation of a double-peaked structure. With a previously estimated nonlinear phase shift exceeding 3.5 rad, the pulse is beyond the uniform spectral broadening regime, where such spectral splitting can be expected. In addition, increased spectral bandwidth indicates a change in TL pulse duration. The curves of TL pulse duration, estimated by inverse Fourier transformation of the corresponding spectrum, are depicted in Figure 23(B, C).

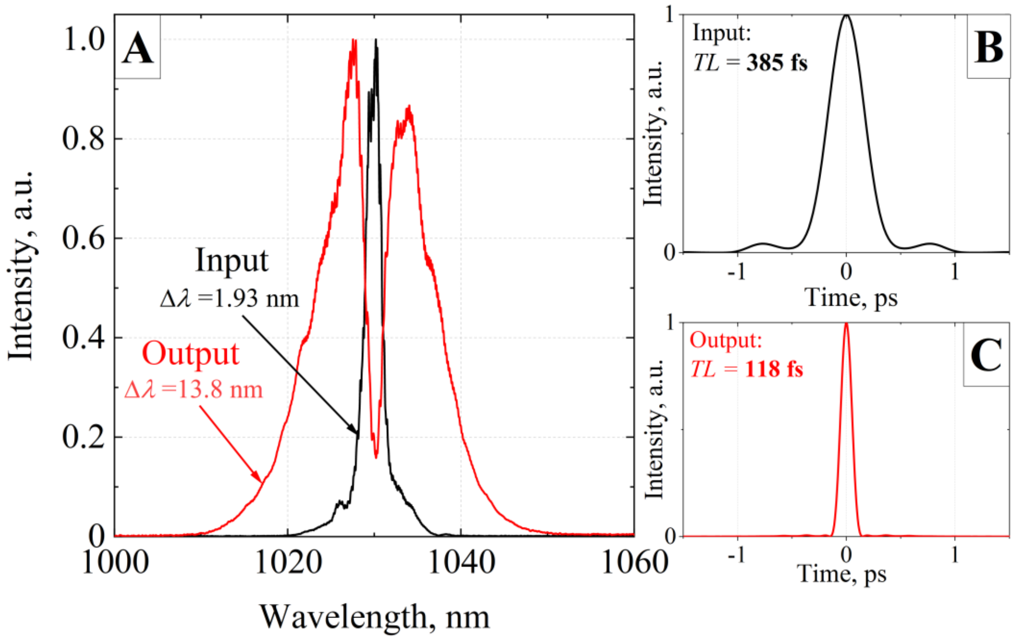

Fig. 23. Measured pulse spectra before and after Kerr-lens filtering (A) and the corresponding transform-limited pulse durations, calculated via inverse Fourier transformation of the spectra for the input pulse (B) and the Kerr-lens-modified pulse (C), with the spectral FWHM marked as $\Delta\lambda$.

Furthermore, FROG analysis was used to provide a more detailed characterization of the pulse in both the temporal and spectral domains. The retrieved temporal and spectral intensity profiles for the input and output pulses are presented in Fig. 24(A, B). The pulse duration after Kerr-lens filtering was reduced by approximately 21% to 298 fs, while the resulting spectral profile is in good agreement with the experimental measurement in Fig. 23, despite a mismatch of the estimated FWHM possibly caused by measurement errors. The reduction in pulse duration confirms the effect of instantaneous Kerr lensing, which, in combination with spatial filtering, suppresses low-intensity temporal components, leading to the pulse shortening.

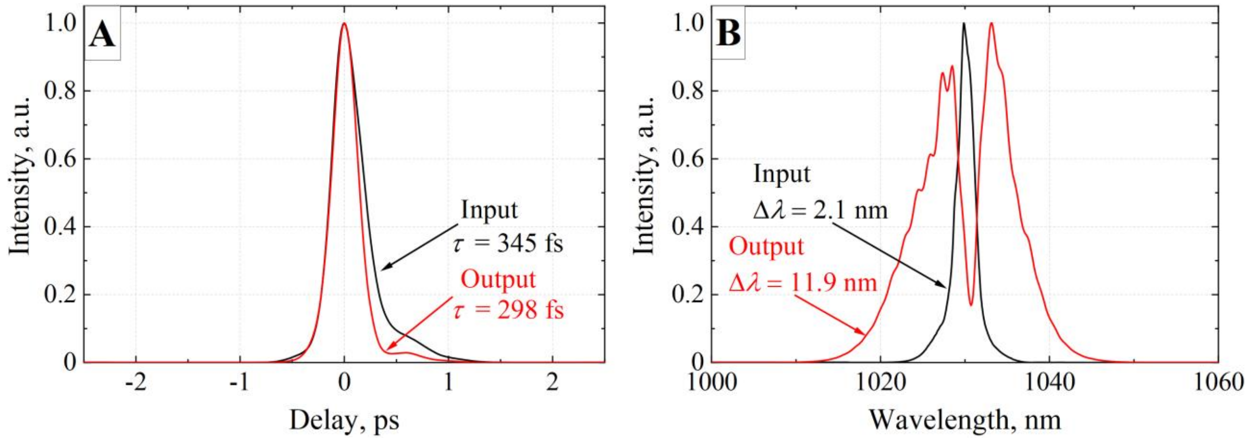

Fig. 24. Pulse temporal envelope (A) and spectrum (B) before and after Kerr-lens filtering scheme, retrieved using FROG analysis, with the spectral FWHM marked as $\Delta\lambda$.

An important consequence of Kerr-lens filtering is the significant spectral broadening of the pulse, theoretically enabling further compression to 118 fs, as depicted in Fig. 23(C). The spectral intensity and phase profiles for the input and the output pulse of the investigated filtering scheme are presented in Fig. 25. The spectral phase of the output pulse exhibits pronounced curvature and was fitted using a Taylor expansion (3) to extract residual dispersion terms. Due to a non-uniform phase distortion near 1030 nm, a second-order (parabolic) fit was adopted as an approximation. The parabolic fit yields a GDD of approximately 7800 fs², indicating that the output pulse is predominantly linearly chirped and may be further compressed. However, higher-order phase distortions at the 1030 nm suggest that efficient compression toward the TL duration is challenging with standard dispersive optics due to limited control over dispersion terms beyond TOD.

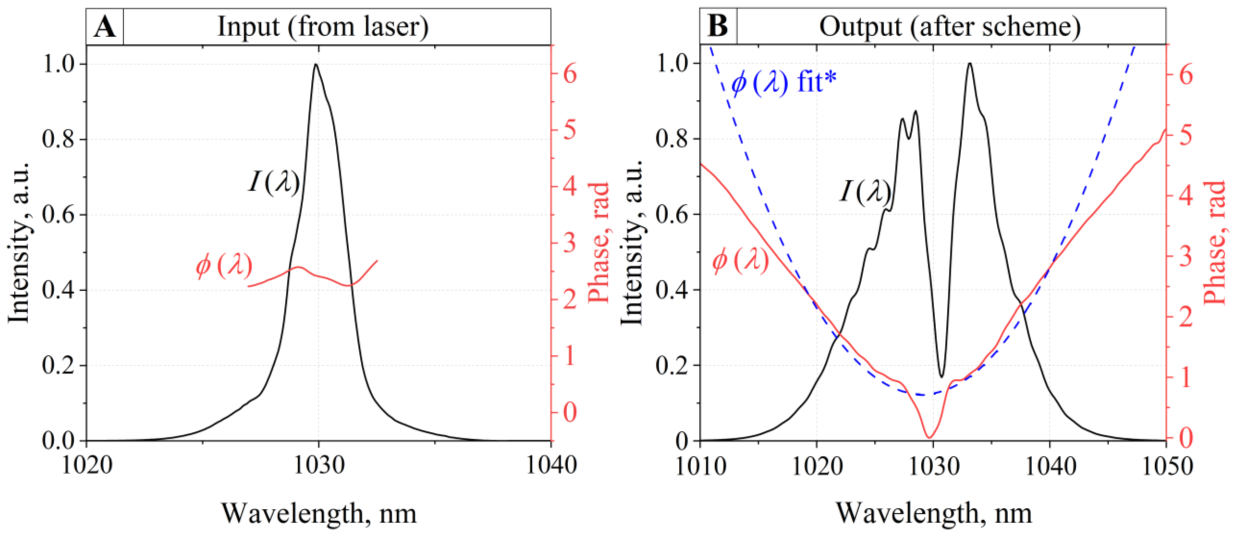

Fig. 25. Spectrum of the input pulse (A) and after Kerr-lens filtering (B), retrieved using FROG analysis. A parabolic fit of the residual spectral phase of the output pulse is shown as a dashed blue curve.

Moreover, the filtered beam profile and the corresponding beam quality (M^2 parameter) were measured to evaluate the beam modification introduced by this method. Firstly, the input beam quality parameter M^2 for a 200 μJ pulse was found to be approximately 1.03. Following, a beam quality analysis was performed after the Kerr lens filtering. The estimated beam quality parameter M^2 for the filtered beam was 1.62 and 1.51 in X and Y axes, respectively. Additionally, in the near field, concentric rings appeared in the beam profile. This indicates severe degradation of the filtered beam quality. The degradation is attributed to strong truncation of the self-focused beam by a small aperture, where edge diffraction introduces high spatial frequencies, increasing beam divergence and degrading the Gaussian beam quality.

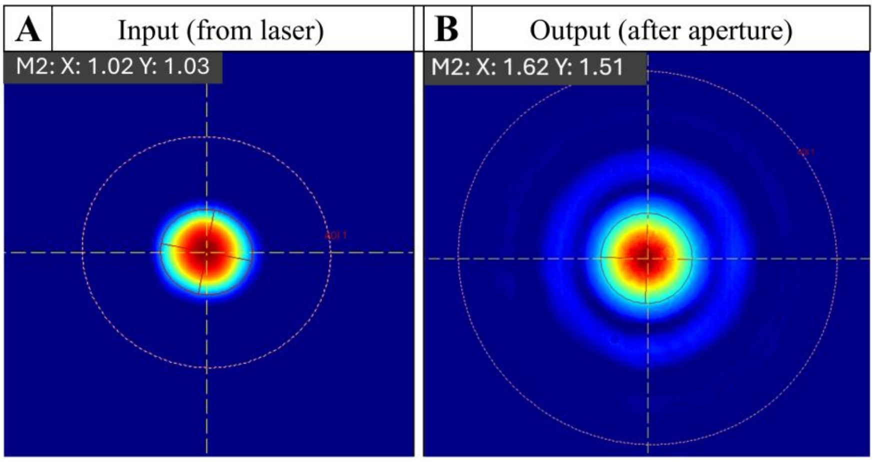

Fig. 26. Near-field beam profile of the laser (A) and after Kerr-lens filtering (B). The M^2 beam quality parameters along the X and Y axes are indicated in the top-left corner of each beam profile.

The results suggest that the external Kerr-lens filtering method can be employed to improve the TC of ultrashort pulses. However, the magnitude of the improvement shall not be overestimated. In the investigation of the filtering scheme, a CE factor of 4 was achieved; however, significant drawbacks for the filtering method were observed. Firstly, the pulse experienced a large nonlinear phase shift (>3 rad), resulting in a broadened pulse spectrum and spectral phase with higher-order distortions. In addition, the filtering using a small aperture introduced heavy clipping of the self-focused beam, which resulted in severe beam quality degradation.

Conclusions

1) The investigated hybrid CPA system demonstrated a temporal contrast (TC) on the order of 10^{-4}, with over 98% of the measured pulse energy contained within the main pulse.
2) The application of CFBG with 2 times reduced reflectivity and GD distortions improved the compressed pulse TC by a factor of 2–3 and reduced the fraction of energy contained in the pulse background relative to the main pulse by approximately a factor of 1.5.
3) The application of a higher-quality CFBG pulse stretcher suppressed the intensity pedestal in the post-compressed 56 fs pulses more effectively, decreasing the pulse background energy fraction by a factor of 2. This indicates that CFBG quality is particularly important for generating high-quality compressed pulses below 100 fs.
4) The investigated external Kerr-lens filtering may be used for a modest TC enhancement; however, the improvement is limited by significant trade-offs, including a large accumulated nonlinear phase shift and beam quality distortion. Therefore, the direct application is strongly constrained without additional pulse clean-up methods.

Literature

[1] M.T. Asaki, C.-P. Huang, D. Garvey, J. Zhou, H.C. Kapteyn, M.M. Murnane, Generation of 11-fs pulses from a self-mode-locked Ti:sapphire laser, Optics Letters, **18**, 977–979 (1993).

[2] W. Lin, R. Liao, J. Wen, Z. Liu, L. Deng, H. Zhang, T. Lai, Sub-10-fs pulse generation directly from a KLM Ti:sapphire laser, Chinese Science Bulletin, **47**, 1050–1052 (2002).

[3] W.F. Krupke, Ytterbium solid-state lasers. The first decade, IEEE Journal of Selected Topics in Quantum Electronics, **6**, 1287–1296 (2000).

[4] C. Hönninger, R. Paschotta, M. Graf, F. Morier-Genoud, G. Zhang, M. Moser, S. Biswal, J. Nees, A. Braun, G.A. Mourou, I. Johannsen, A. Giesen, W. Seeber, U. Keller, Ultrafast ytterbium-doped bulk lasers and laser amplifiers, Applied Physics B, **69**, 3–17 (1999).

[5] R. Paschotta, J. Nilsson, A.C. Tropper, D.C. Hanna, Ytterbium-doped fiber amplifiers, IEEE Journal of Quantum Electronics, **33**, 1049–1056 (1997).

[6] Z. Kovács, K. Bali, B. Gilicze, S. Szatmári, I.B. Földes, Reflectivity and spectral shift from laser plasmas generated by high-contrast, high-intensity KrF laser pulses, Philosophical Transactions of the Royal Society A, **378**, 20200043 (2020).

[7] A. Kessel, V.E. Leshchenko, O. Jahn, M. Krüger, A. Münzer, A. Schwarz, V. Pervak, M. Trubetskov, S.A. Trushin, F. Krausz, Z. Major, S. Karsch, Relativistic few-cycle pulses with high contrast from picosecond-pumped OPCPA, Optica, **5**, 434–442 (2018).

[8] F. Azizian, A. Hasanbeigi, M.J. Jafari, S. Rezaei, Pre-plasma shaping via picosecond laser contrast: A hybrid simulation study of proton acceleration in TNSA, Physics of Plasmas, **32**, 113104 (2025).

[9] L. Veselis, T. Bartulevicius, K. Madeikis, A. Michailovas, N. Rusteika, Compact 20 W femtosecond laser system based on fiber laser seeder, Yb:YAG rod amplifier and chirped volume Bragg grating compressor, Optics Express, **26**, 31873–31879 (2018).

[10] S.S. Aleshkina, Y.P. Yatsenko, M.Y. Salganskii, D.S. Lipatov, A.K. Senatorov, A.V. Tausenev, D.V. Shepelev, M.M. Bubnov, A.N. Guryanov, M.E. Likhachev, High-peak-power femtosecond pulse generation by nonlinear compression in a Yb-doped hybrid fiber, IEEE Photonics Journal, **11**, 1–11 (2019).

[11] A. Braun, S. Kane, T. Norris, Compensation of self-phase modulation in chirped-pulse amplification laser systems, Optics Letters, **22**, 615–617 (1997).

[12] J. Limpert, F. Röser, T. Schreiber, A. Tünnermann, High-power ultrafast fiber laser systems, IEEE Journal on Selected Topics in Quantum Electronics, **12**, 233–244 (2006).

[13] D. Li, H. Jussila, Y. Wang, G. Hu, T. Albrow-Owen, R.C.T. Howe, Z. Ren, J. Bai, T. Hasan, Z. Sun, Wavelength and pulse duration tunable ultrafast fiber laser mode-locked with carbon nanotubes, Scientific Reports, **8**, 2738 (2018).

[14] V. Shumakova, V.F. Pecile, J. Fellinger, M. Leskowschek, P.E.C. Aldia, A.S. Mayer, L.W. Perner, S. Salman, M. Fan, P. Balla, S. Schilt, C.M. Heyl, I. Hartl, G. Porat, O.H. Heckl, Spectrally tunable high-power Yb:fiber chirped-pulse amplifier, Photonics Research, **10**, 2309–2316 (2022).

[15] X. Cao, F. Li, Y. Wang, H. Zhao, W. Zhao, Q. Li, J. Xing, W. Wen, J. Si, 2.6 GW, mJ-class high-energy femtosecond laser system based on Yb:YAG single-crystal fiber amplifier, Infrared Physics & Technology, **144**, 105643 (2025).

[16] A. Kazakevičius, R. Burokas, R. Danilevičius, A. Michailovas, Ultrafast 10 mJ, 100 W laser system featuring a directly laser written depolarization compensation element, Optics Express, **32**, 15326–15335 (2024).

[17] C.T. Pan, Y.M. Hwang, C.W. Hsieh, Fast fabrication of silicon based microstructures using 355 nm UV laser, Materials Science and Technology, **21**, 1344–1348 (2005).

[18] K.C. Phillips, H.H. Gandhi, E. Mazur, S.K. Sundaram, Ultrafast laser processing of materials: a review, Advances in Optics and Photonics, **7**, 684–712 (2015).

[19] X. Liu, J. Lægsgaard, D. Turchinovich, Highly-stable monolithic femtosecond Yb-fiber laser system based on photonic crystal fibers, Optics Express, **18**, 15475–15483 (2010).

[20] X. Cao, F. Li, D. Song, Y. Wang, Q. Li, H. Zhao, W. Zhao, W. Wen, J. Si, Environmentally stable all-fiber femtosecond laser for industrial application based on a SESAM mode-locked ytterbium-doped laser, Microwave and Optical Technology Letters, **66**, e34119 (2024).

[21] T. Bartulevičius, Compact high pulse energy fiber laser systems for industrial and scientific applications, PhD thesis, Vilnius University, Vilnius (2021).

[22] M.E. Fermann, V.I. Kruglov, B.C. Thomsen, J.M. Dudley, J.D. Harvey, Self-similar propagation and amplification of parabolic pulses in optical fibers, Physical Review Letters, **84**, 6010–6013 (2000).

[23] G. Imeshev, I. Hartl, M.E. Fermann, Chirped pulse amplification with a nonlinearly chirped fiber Bragg grating matched to the Treacy compressor, Optics Letters, **29**, 679–681 (2004).

[24] D.N. Schimpf, E. Seise, J. Limpert, A. Tünnermann, The impact of spectral modulations on the contrast of pulses of nonlinear chirped-pulse amplification systems, Optics Express, **16**, 10664–10674 (2008).

[25] F. Ouellette, H. Wang, Measurement of group delay ripples of chirped fiber Bragg gratings for CPA lasers, and their effect on performance, Photonics, **11**, 333 (2024).

[26]. D.N. Schimpf, E. Seise, J. Limpert, A. Tünnermann, Decrease of pulse-contrast in nonlinear chirped-pulse amplification systems due to high-frequency spectral phase ripples, Optics Express, **16**, 8876–8886 (2008).

[27] Y. Xu, Y. Leng, X. Guo, X. Zou, Y. Li, X. Lu, C. Wang, Y. Liu, X. Liang, R. Li, Z. Xu, Pulse temporal quality improvement in a petawatt Ti:sapphire laser based on cross-polarized wave generation, Optics Communications, **313**, 175–179 (2014).

[28] L. Yu, Y. Xu, S. Li, Y. Liu, J. Hu, F. Wu, X. Yang, Z. Zhang, Y. Wu, P. Bai, X. Wang, X. Lu, Y. Leng, R. Li, Z. Xu, Investigation of the temporal contrast evolution in a 10-PW-level Ti:sapphire laser facility, Optics Express, **27**, 8683–8695 (2019).

[29] D.N. Papadopoulos, P. Ramirez, K. Genevrier, L. Ranc, N. Lebas, A. Pellegrina, C. Le Blanc, P. Monot, L. Martin, J.P. Zou, F. Mathieu, P. Audebert, P. Georges, F. Druon, High-contrast 10 fs OPCPA-based front end for multi-PW laser chains, Optics Letters, **42**, 3530–3533 (2017).

[30] A. Kim, I. Dey, A. Bespaly, P. Komm, A. Shaham, J. Papeer, M. Botton, A. Zigler, Investigation of pre-pulse effects on ultrashort-pulse laser interaction with structured targets, Applied Sciences, **15**, 237 (2025).

[31] T.Z. Esirkepov, J.K. Koga, A. Sunahara, T. Morita, M. Nishikino, K. Kageyama, H. Nagatomo, K. Nishihara, A. Sagisaka, H. Kotaki, T. Nakamura, Y. Fukuda, H. Okada, A.S. Pirozhkov, A. Yogo, M. Nishiuchi, H. Kiriyama, K. Kondo, M. Kando, S.V. Bulanov, Prepulse and amplified spontaneous emission effects on the interaction of a petawatt class laser with thin solid targets, Nuclear Instruments and Methods in Physics Research Section A, **745**, 150–163 (2014).

[32] A. Wang, A. Das, D. Grojo, Temporal-contrast imperfections as drivers for ultrafast laser modifications in bulk silicon, Physical Review Research, **2**, 033023 (2020).

[33] M. Kalashnikov, K. Osvay, W. Sandner, High-power Ti:sapphire lasers: temporal contrast and spectral narrowing, Laser and Particle Beams, **25**, 219–223 (2007).

[34] Y. Xu, Y. Leng, L. Lin, W. Wang, Y. Huang, R. Li, Z. Xu, Amplified spontaneous emission contrast of CPA laser, Chinese Optics Letters, **8**, 123–125 (2010).

[35] J. Dong, M. Bass, Y. Mao, P. Deng, F. Gan, Dependence of the Yb^{3+} emission cross section and lifetime on temperature and concentration in yttrium aluminum garnet, Journal of the Optical Society of America B, **20**, 1975–1979 (2003).

[36] A. Shirakov, Z. Burshtein, Y. Shimony, E. Frumker, A.A. Ishaaya, Radiative and non-radiative transitions of excited Ti^{3+} cations in sapphire, Scientific Reports, **9**, 19108 (2019).

[37] A.-L. Viotti, S. Alisauskas, H. Tünnermann, E. Escoto, M. Seidel, K. Dudde, B. Manschwetus, I. Hartl, C.M. Heyl, Temporal pulse quality of a Yb:YAG burst-mode laser post-compressed in a multi-pass cell, Optics Letters, **46**, 4686–4689 (2021).

[38] Z. Refaeli, G. Marcus, Y. Shamir, A simple method for pulse contrast enhancement via self-focusing, High Power Laser Science and Engineering, **12**, e18 (2024).

[39] J. Song, L. Shen, J. Sun, Y. Peng, Y. Leng, Temporal contrast enhancement by nonlinear elliptical polarization rotation in a multi-pass cell, High Power Laser Science and Engineering, **10**, e28 (2022).

[40] A. Renault, F. Augé-Rochereau, T. Planchon, P. D'Oliveira, T. Auguste, G. Chériaux, J.P. Chambaret, ASE contrast improvement with a non-linear filtering Sagnac interferometer, Optics Communications, **248**, 535–541 (2005).

[41] R.C. Shah, R.P. Johnson, T. Shimada, K.A. Flippo, J.C. Fernandez, B.M. Hegelich, High-temporal contrast using low-gain optical parametric amplification, Optics Letters, **34**, 2273–2275 (2009).

[42] Y. Huang, C. Zhang, Y. Xu, D. Li, Y. Leng, R. Li, Z. Xu, Ultrashort pulse temporal contrast enhancement based on noncollinear optical-parametric amplification, Optics Letters, **36**, 781–783 (2011).

[43] A. Jullien, S. Kourtev, O. Albert, G. Chériaux, J. Etchepare, N. Minkovski, S.M. Saltiel, Highly efficient temporal cleaner for femtosecond pulses based on cross-polarized wave generation in a dual crystal scheme, Applied Physics B, **84**, 409–414 (2006).

[44] J. Song, L. Shen, J. Sun, Y. Peng, Y. Leng, Temporal contrast enhancement via nonlinear elliptical polarization rotation in a solid thin plate, Optics Express, **30**, 26297–26305 (2022).

[45] J. Buldt, M. Müller, R. Klas, T. Eidam, J. Limpert, A. Tünnermann, Temporal contrast enhancement of energetic laser pulses by filtered self-phase-modulation-broadened spectra, Optics Letters, **42**, 3761–3764 (2017).

[46] F. Zhang, A. Pelekanidis, A. Karpavicius, M. Gouder, J. Seifert, K. Eikema, S. Witte, Characterizing post-compression of mJ-level ultrafast pulses via loose focusing in a gas cell, Optics Express, **32**, 40990–41003 (2024).

[47] J.F. Hergott, F. Réau, O. Tcherbakoff, F. Lepetit, N. Lericheux, M. Guer, H. Marroux, R. Géneaux, A. Tyagi, R. Cazali, P. Nonnon, D. Bresteau, T. Ruchon, P. Salières, T. Auguste, Experimental and numerical study of direct sub-20fs multi-pass-cell post-compression of up to 4mJ, 80W Yb-based lasers, Applied Physics B, **131**, 56 (2025).

[48] T. Nagy, P. Simon, L. Veisz, High-energy few-cycle pulses: post-compression techniques, Advances in Physics: X, **6**, 1845795 (2021).

[49] M. Ivanov, E. Doiron, M. Scaglia, P. Abdolghader, G. Tempea, F. Légaré, C.A. Trallero-Herrero, G. Vampa, B. Schmidt, Advancing high-power hollow-core fiber pulse compression, IEEE Journal of Selected Topics in Quantum Electronics, **30**, 5100310 (2024).

[50] C.-H. Lu, W.-H. Wu, S.-H. Kuo, J.-Y. Guo, M.-C. Chen, S.-D. Yang, A.H. Kung, Greater than 50 times compression of 1030 nm Yb:KGW laser pulses to single-cycle duration, Optics Express, **27**, 15638–15648 (2019).

[51] J.E. Beetar, S. Gholam-Mirzaei, M. Chini, Spectral broadening and pulse compression of a 400 μJ, 20 W Yb:KGW laser using a multi-plate medium, Applied Physics Letters, **112**, 051102 (2018).

[52] A.-L. Viotti, S. Alisauskas, H. Tünnermann, E. Escoto, M. Seidel, K. Dudde, B. Manschwetus, I. Hartl, C.M. Heyl, Temporal pulse quality of a Yb:YAG burst-mode laser post-compressed in a multi-pass cell, Optics Letters, **46**, 4686–4689 (2021).

[53] J.-C. Diels, W. Rudolph, Ultrashort Laser Pulse Phenomena: Fundamentals, Techniques, and Applications on a Femtosecond Time Scale, (Elsevier Academic Press, Amsterdam, 2006).

[54] J. Ma, P. Yuan, J. Wang, G. Xie, H. Zhu, L. Qian, Single-shot cross-correlator for pulse-contrast characterization of high peak-power lasers, High Power Laser Science and Engineering, **6**, e61 (2018).

[55] R. Trebino, P. Bowlan, P. Gabolde, X. Gu, S. Akturk, M. Kimmel, Measuring everything you've ever wanted to know about an ultrashort light pulse, European Virtual University (2008).

[56] D.J. Kane, R. Trebino, Single-shot measurement of the intensity and phase of an arbitrary ultrashort pulse by using frequency-resolved optical gating, Optics Letters, **18**, 823–825 (1993).

Ultratrumpųjų impulsų laikinės kokybės analizė hibridiniame lazeryje su šviesolaidiniu užkrato šaltiniu

Adomas Petrauskas

Santrauka

Ultratrumpieji lazerių impulsai yra itin svarbūs tiek fundamentiniuose tyrimuose, tiek lazeriniuose taikymuose – nuo didelės energijos impulsų tyrimų iki precizinio medžiagų apdirbimo. Dalyje taikymų didelę reikšmę turi laikinė impulso kokybė, dažnai įvertinama kaip laikinis kontrastas – pagrindinio impulso intensyvumo ir satelitinų laikinių struktūrų intensyvumo santykis. Siekiant užtikrinti aukštą impulsų kokybę, hibridinėse ultratrumpųjų impulsų sistemose dažnai derinamos kelios stiprinimo pakopos, skirtos padidinti išėjimo galią, išlaikant aukštą impulsų laikinę ir erdvinę kokybę. Šviesolaidiniu užkratu paremtose čirpuotų impulsų stiprinimo (angl. Chirped Pulse Amplification, CPA) sistemose laikinio kontrasto prastėjimas yra nulemtas netiesinės fazės kaupimosi bei aukštesnių eilių dispersijos nekompensavimo. Netiesinės fazės kaupimasis, gali pasireikšti stiprinimo pakopose, kai impulsas turi pakankamą smailinį intensyvumą fazinei savimoduliacijai vykti. Tuo pat metu taikomi dispersiniai komponentai gali įnešti aukštesnių eilių dispersiją ar spektrinės amplitudės bei grupinio vėlinimo iškraipymus. Taigi, išsamus impulso laikinių savybių tyrimas ir komponentų analizė yra būtina siekiant išsiaiškinti laikinio kontrasto prastėjimo mechanizmus hibridinėse CPA sistemose.

Šio darbo tikslas – charakterizuoti hibridinį lazerį su šviesolaidiniu užkrato šaltiniu ir impulsų plėtimui panaudojus aukštesnės kokybės čirpuotą šviesolaidinę Brego gardelę (angl. chirped fiber Bragg grating, CFBG), įvertinti mažesnių atspindžio spektro ir grupinio vėlinimo iškraipymų įtaką suspausto impulso kokybei.

Naudojant didelio dinaminio diapazono trečios eilės autokoreliatorių, sistemos išėjime nustatytas maždaug 10^{-4} eilės impulsų laikinis kontrastas, kuris darbe apibrėžiamas kaip impulso smailės ir intensyviausio laikinio satelito intensyvumų santykis. Be to, integruojant autokoreliacinį signalą pasirinktame vėlinimo lange nustatyta, kad maždaug 98 % impulso energijos yra sutelkta pagrindinės smailės ±1 ps laikiniame intervale, palyginti su energijos fonu ±30 ps vėlinimo lange. Šviesolaidiniame užkrate CFBG pakeitus aukštesnės kokybės komponentu, pasižyminčiu mažesniais spektriniais ir grupinio vėlinimo iškraipymais, impulso laikinis kontrastas pagerintas maždaug 2-3 kartus. Be to, impulso fono energijos dalis pagrindinio impulso energijos atžvilgiu sumažėjo 1,5 karto, kas patvirtina CFBG kokybės įtaką suspausto impulso laikinei kokybei. Papildomai atlikus išorinę impulsų spūdą iki 56 fs, trečios eilės autokoreliatoriumi ir dažninės skyros optinės sklendės (angl. frequency-resolved optical gating, FROG) metodu buvo patvirtinta,

jog aukštesnė CFBG impulsų plėstuvo kokybė 6 kartus išoriškai suspaustam impulsui turėjo didesnę įtaką ir sumažino fono energijos dalį 2 kartus.

Be to, sistemos išejime išbandytas išorinis laikinio kontrasto gerinimo metodas pagrįstas Kero lęšio filtravimu. Nustatyta, jog šis metodas leidžia 4 kartus pagerinti impulso laikinį kontrastą, tačiau kartu atliekama reikšminga impulso spektro modifikacija bei sugadinama pradinė pluošto kokybė. Galima teigti, jog susidarantys spektriniai ir erdviniai iškraipymai riboja tiesioginį Kero lęšio filtravimo taikymą laikiniam kontrastui gerinti CPA sistemų išėjime.

Apibendrinant, rezultatai rodo, jog CFBG impulsų plėstuvų kokybė yra svarbus veiksnys CPA sistemose su šviesolaidiniu užkrato šaltiniu, todėl, siekiant aukštos ultratumpųjų impulsų kokybės, atsiranda būtinybė naudoti CFBG komponentus su tolygesniais atspindžio spektro ir grupinio vėlinimo profiliais.